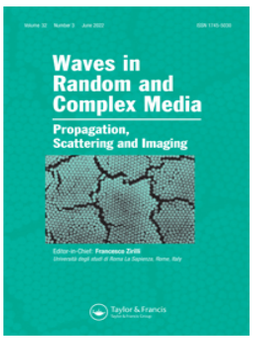

Taylor & Francis
Taylor & Francis Group

Waves in Random and Complex Media

ISSN: (Print) (Online) Journal homepage: https://www.tandfonline.com/loi/twrm20

Assessment of thermal performance of hybrid nanofluid flow in a tilted porous enclosure by imposing partial magnetic fields

Milan K. Mondal, Nirmalendu Biswas, Dipak Kumar Mandal, Nirmal K. Manna & Ali J. Chamkha

To cite this article: Milan K. Mondal, Nirmalendu Biswas, Dipak Kumar Mandal, Nirmal K. Manna & Ali J. Chamkha (2022): Assessment of thermal performance of hybrid nanofluid flow in a tilted porous enclosure by imposing partial magnetic fields, Waves in Random and Complex Media, DOI: 10.1080/17455030.2022.2066220

To link to this article: https://doi.org/10.1080/17455030.2022.2066220

Published online: 28 Apr 2022.

WAVES IN RANDOM AND COMPLEX MEDIA
https://doi.org/10.1080/17455030.2022.2066220

Taylor & Francis
Taylor & Francis Group

Assessment of thermal performance of hybrid nanofluid flow in a tilted porous enclosure by imposing partial magnetic fields

Milan K. Mondal [a], Nirmalendu Biswas [b], Dipak Kumar Mandal [c], Nirmal K. Manna [d] and Ali J. Chamkha [e]

[a]Department of Mechanical Engineering, MSG Polytechnic, Paschim Medinipur, India; [b]Department of Power Engineering, Jadavpur University, Salt Lake, Kolkata, India; [c]Department of Mechanical Engineering, College of Engineering and Management, Kolaghat, West Bengal, India; [d]Department of Mechanical Engineering, Jadavpur University, Salt Lake, Kolkata, India; [e]Faculty of Engineering, Kuwait College of Science and Technology, Doha District, Kuwait

ABSTRACT

A novel approach of implementation of a partial active magnetic field in a slanting porous cavity packed with hybrid nanofluid has a significant influence on the various types of passive controlling of the transport phenomena. The magnetohydrodynamic (MHD) flow coupled with other multiphysics comes across widespread applications in health and medical science, electronics, others. Imposing magnetic field, treatment of tumor tissues is a promising technique, which needs an in-depth analysis of thermal performance. In this context, the present study explores a novel implementation of the partial magnetic field induced on a differentially heated inclined porous square enclosure containing $Cu-Al_2O_3$/water hybrid nanofluid. The partial magnetic field is imposed using varying effective width and the allocation impacts of this partial magnetic field on the inclined cavity have been investigated systematically. The width, as well as positional impacts of the applied partial magnetic fields, has been scrutinized thoroughly. The coupled transport equations are used for the solution by the finite volume technique (FVM) for a selective range of variables like Darcy-Rayleigh number (Ra_m), Hartmann number (Ha), Darcy number (Da), the concentration of hybrid nanofluid (ζ) and cavity angle (γ). The investigation exposes that the partial magnetic fields with cavity inclination have substantial effects on the heat transport mechanism. The study indicates that adjusting the position and width of the imposed magnetic fields, cavity angle, and involved pertinent parameters can significantly modulate the local as well as global transport phenomena under the multi-physical scenario. This technique allows less reduction in heat transfer, which is $\sim$15% (with partial magnetic field) and $\sim$30% (with whole domain magnetic field) relative to the no-magnetic field.

ARTICLE HISTORY
Received 14 October 2021
Accepted 6 April 2022

KEYWORDS
Partial magnetic fields; hybrid nanofluid; cavity angle; porous medium; heat transfer

CONTACT Nirmalendu Biswas biswas.nirmalendu@gmail.com

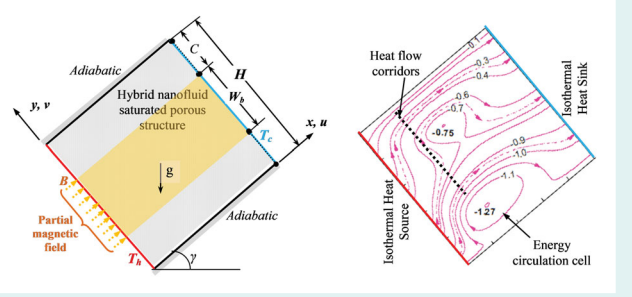

Highlights

- The impact of a partially active magnetic field on thermal convection in a typical porous inclined cavity packed with a hybrid nanofluid is analyzed.
- The positional shifting and width of the spatially active magnetic field for the various parameters are illustrated using streamlines, isotherms, heatlines, and Nusselt numbers.
- The orientation of the enclosure under the partial magnetic fields significantly alters the overall thermal performance of the enclosure.
- The magnetic field intensity, porous structure permeability, volume concentrations of hybrid nanoparticles comprehensively persuade fluid and heat flow features.
- With this technique reduction in heat transfer is less, which is $\sim$ 15% (with partial magnetic field), and $\sim$ 30% (with whole domain magnetic field) relative to the no-magnetic field.

Nomenclature

B	magnetic fields (N A^{-1} m^{-2})
C	width of inactive zones (m)
Da	Darcy number
F_c	Forchheimer coefficient
g	gravitational acceleration (m s^{-2})
H	cavity height (m)
Ha	Hartmann number
K	porous medium permeability (m^2)
Nu	Nusselt number (average)
P	unitless pressure
Pr	Prandtl number
Ra	fluid-based Rayleigh number
Ra_m	Darcy–Rayleigh number
t	time (s)
T	temperature (K)
u, v	components of velocity (m s^{-1})
U, V	non-dimensional velocities
x, y	Cartesian coordinates (m)
X, Y	non-dimensional coordinates
W_b	active magnetic field width

Greek symbols

α	thermal diffusivity ($m^2\,s^{-1}$)
β	thermal expansion coefficient (K^{-1})
ε	porosity
θ	non-dimensional temperature
λ_B	magnetic field parameter
μ	dynamic viscosity ($kg\,m^{-1}\,s^{-1}$)
ν	kinematic viscosity ($m^2\,s^{-1}$)
ρ	density ($kg\,m^{-3}$)
τ	non-dimensional time
ζ	hybrid nanoparticles volume fraction
ψ	stream function

Subscripts

a	ambient
c	cold
f	base fluid
h	hot
l	local
max	maximum
s	solid

1. Introduction

The fastest growth in the technology and electronic industry allows the manufacturer to develop various sophisticated devices ranging from large to mini scale based on demand without compromising its operational efficiency. However, precise control of the transport process in a system/ maneuver is a major task to the maker. In this contest, when appropriate electrically conducting fluids are used as a working medium, an externally generated magnetic field can efficiently modulate the transport process in critical applications. In order to increase more controllability of such a magneto-thermal device, the application of a novel technique of spatially active partial magnetic field is a promising technique in recent years [1–3]. A thermal transport phenomenon in the existence of external magnetic force is termed as magnetohydrodynamics (MHD). The behavior of the magnetic field finds numerous applications in diverse fields like biomedical technology ranging from separation of cells, targeted drug delivery, magnetic endoscopy, tumor and cancer treatment through magnetic hyperthermia, controlling of blood flow during surgery, bio-waste fluids transport etc. [4–8]. The application of the magnetic fields can also be found in industries coupled with various multiphysics involving porous structure (solids with pores), nanofluid/ hybrid nanofluid (suspension of nano-size metallic and non-metallic oxides in suitable a carrier fluid), etc. Some examples are MEMs, cooling of electronic circuits, material processing, plasma welding, anti-vibration devices, microfluidic devices, and others [9–20]. A comprehensive review study on the potentials of the magnetic field application is reported by

Kabeel [21], Kumar and Subudhi [22], Pordanjani et al. [23], Nguyen-Thoi et al. [24], and others. There are other classes of works involving magnetic field, nanofluid/ hybrid nanofluid, and porous substance, which demonstrated the thermal performance of the geometries under the various controlling parametric effects with obstruction [25]. Buoyant convection in a trapezoidal shaped-cavity has also been studied considering non-uniform heating conditions [26]. Considering classical square cavity nanofluidic magnetothermal convetion has also been investigated by several researchers [27,28]. Nanofluidic mixed thermal convection in various geometries has also been studied in refs. [29–34].

Transport phenomena in a magneto-thermal system involving various multiphysics become more complex depending upon the geometries and associated boundary conditions. Modeling as well as simulation of such a problem is a critical challenge to the designer. Of course, researchers are persistently giving their devotion to improving the transport process in various complex systems/ geometries. For an example, magneto-thermal convection in an enclosure studied considering line dipole [1,35], uniform magnetic fields [36–40], and sloped magnetic field [39], intermittently active magnetic field [3,4], alternating magnetic fields [6], periodic magnetic field [40–42], etc. Applying a partially active magnetic field, Jalil et al. [43] scrutinized the buoyancy-induced thermo-magnetic convection of molten gallium in an enclosure heated differentially. It is found that thermo-fluid behavior is essentially modulated by the strength of the partially functional magnetic field and the oscillating pattern of the heat transfer rate disappears. The concept of the partially active non-uniform magnetic field has been adopted by Szabo and Früh [44] and examined the thermo-magnetic convection of magnetic fluid in a differentially heated enclosure. Their study reveals that magnetic force can dominate buoyancy force and accompanying heat transfer. Later Geridonmez and Oztop applied the partial magnetic field diagonally from the corner of an air-filled cavity [45], horizontally in an alumina-oxide-water nanofluid-filled cavity [46], and horizontally in an air-packed porous cavity [2] differentially heated enclosure undergoing free-convective heat transfer. All these investigations noticeably revealed the impact of partial magnetic fields on thermomagnetic convection, which is influenced by the location, width, and intensity of the imposed partial magnetic field. Very recently, Manna et al. [3] reported about a concept of multi-banded magnetic field (four-bands, two-bands, and single-band having equal active length) applied intermittently in a hybrid nanofluid packed porous cavity heated differentially. The same group [47] has also been investigated the convective transport of hybrid nanoliquid through porous medium filled in a linearly heated enclosure applying four banded magnetic fields. Both the investigation has reported that application of the partially energized magnetic field is always a better choice for a system and energy-efficient in respect of the whole imposed magnetic field. Controllability of the transport process is much more.

The consequence of partial magnetic field on thermomagnetic convection of CNT- nanoliquid in a cubical enclosure is examined numerically Al-Rashed et al. [48]. They stated that the location of a partially active magnetic field can significantly regulate the thermal behavior within the enclosure. Song and Tagawa [49] examined the impact of permanent magnet location and its strength on the transport in an oxygen-filled cavity. They presented an overall heat transfer improvement of $\sim$17.9% at a higher magnetic strength. They also noted that the increase in overall heat transfer is higher with magnet position closer to the heated wall. Utilizing magnetic quadrupole Jiang et al. [50] scrutinized magnetic convection porous cavity filled with air. Heat transfer rises with increasing magnetic

field intensity under the no gravity condition and a reverse trend with gravity condition. Recently, Izadia et al. [51] studied the convective phenomena of Ag–MgO/water hybrid nanoliquid flow through a porous medium in a left hot and side cooled cavity with a tilted periodic magnetic field. They indicated that periodic magnetic field non-monotonically affects the heat transfer. The investigation of magnetohydrodynamic convection of non-homogeneous nanofluid has also been investigated in an enclosure of hexagonal shape subjected to a non-uniform magnetic field (using line dipole) and found that heat and mass transfer is growing function of magnetic number.

From the generic widespread literature survey, the importance of magnetohydrodynamic convection is well recognized in various types of geometries. However, there partial magnetic field has been addressed in some of the studies without emphasizing the local transport phenomena, which plays a key role in modulating the undergoing processes. Thus, the purpose of this work is to explore the thermomagnetic convection coupled to multiphysical conditions adopting a partially active magnetic field instead of the completely acted magnetic field towards improving the controllability of the transport process. To illustrate this, a spatially active partial field is applied perpendicularly to a differentially hot oblique porous enclosure packed with Cu-Al_2O_3/water hybrid nanoliquid. To assess the influence of the partial magnetic field, the length of the active zone of magnetic fields is varied and compared with the full-domain magnetic field and without any magnetic field cases. The local heat transport mechanisms are visualized through Kimura and Bejan's heatlines [52,53]. The study is conducted for a wide range of involved parameters like Hartmann number (Ha), the width of the active magnetic field (W_b), Darcy number (Da), Darcy-Rayleigh number (Ra_m), hybrid nanofluid concentration (ζ), and cavity inclination angle (γ). The concept of the study will help the researchers to improve their knowledge of a magneto-thermo-fluidic system involving various multiphysical conditions for many sophisticated applications.

In general, this study contributes a lot to understanding the thermo-fluid phenomena of a hybrid nanofluid flow in a porous medium filled oblique cavity, in consideration of the partially active magnetic fields. The investigation is undertaken to explore the impact of width as well as positional effects of the applied partial magnetic field on the overall thermo-fluid flow phenomena in an oriented cavity heated differentially. Furthermore, the benefit of imposing a partial magnetic field over a whole-domain magnetic field is also explored, which shows a lesser reduction in heat transfer (compared to a whole-domain magnetic field). The thermo-fluid phenomena under the partial magnetic field are also modulated significantly compared to the no-magnetic field and whole-domain magnetic field, which is very useful for controlling the thermal transport process. A mathematical correlation is also developed through regression analysis, to predict the overall heat transfer involving various controlling parameters. This way of study can provide design and operation data for the proper selection of dimensions of the cavity for achieving superior heat transfer in a typical thermal system.

2. Description of geometry and mathematical treatment

The schematic diagram of spatially active partial magnetic fields (over the width W_b) is shown in Figure 1. For the configuration (specified as in Figure 1(a)), the effective length W_b of uniform magnetic fields (of intensity B) is distributed normally to the left side equally

about the middle-plane of the cavity. The enclosure, left heated and right cold walls, other walls are adiabatic, is inclined with the horizontal axis and the cavity is allowed to rotate in the anticlockwise direction. The oblique cavity is packed with a porous substance and water-based Cu−Al_2O_3 hybrid nanoliquid. Hot plume is generated due to localized heating of the left sidewall, it rises upward and travels towards the right side after being blocked by the upper adiabatic wall. On the right side, the hot plume cools due to losing its heat to the cooled wall, and then the fluid reaches the bottom portion of the heated wall after being directed by the lower adiabatic wall. As a result, the clockwise circulating cell is formed. A typical distribution of heatlines is elucidated in Figure 1(b). It illustrates the active passages of heat energy flow (in between the hot wall to cold wall) and a passive energy recirculation cell when passing through the cavity. The useful implementation of such partially active magnetic fields could be simply generated by properly intended electrically wound coils [54].

To solve the coupled complex problem involving various multiphysical conditions (like the temperature gradient, porous structure, hybrid nanofluid, cavity inclination, and partial magnetic field), it is presumed that Boussinesq approximation is valid, the hybrid nanofluid flow is steady, incompressible, two-dimensional, and Newtonian. The porous substance is homogeneous having uniform openings, which allows for adopting a single-phase approach for modeling the porous medium adopting the Brinkman-Forchheimer-Darcy model [55–57]. The mixture of Cu and Al_2O_3 nanoparticles (with a constant dia $\sim$1 nm and of spherical shape) is evenly distributed in the carrier fluid water (having Pr = 5.83) without any agglomeration or sedimentation. It is noteworthy to mention that, for obtaining heightened electrical and thermal conductivities (compared to base fluid), the copper-alumina (Cu and Al_2O_3) nanoparticles are suspended in the base fluid to partially counteract the adverse effect of the Lorentz force (which causes damping of flow and heat transfer). Furthermore, in this study experimentally available data of fluid properties (especially dynamic viscosity, and thermal conductivity of Cu and Al_2O_3 nanoparticles mixed hybrid nanofluid) are utilized, which allows predicting more accurate or realistic thermal behavior. In fact, there exist more numbers of research articles using Cu-Al_2O_3-water hybrid nanofluid for applicability in a wider area [58–60].

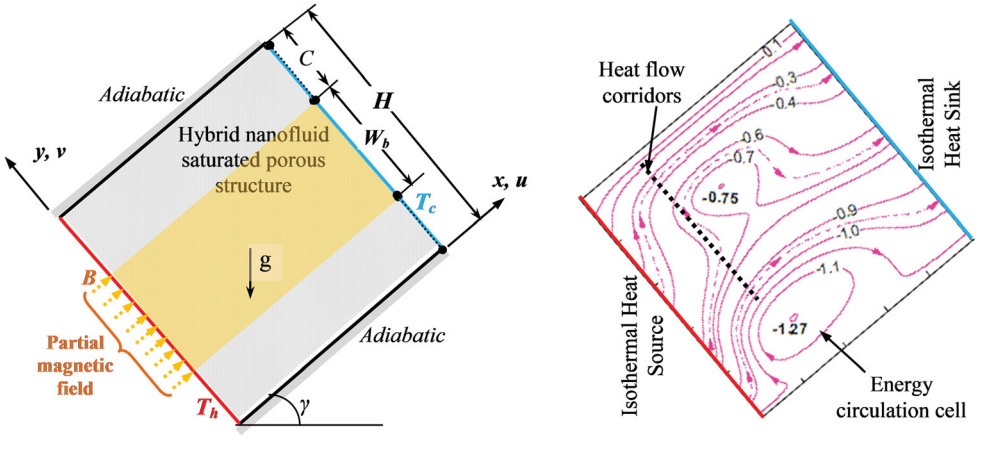

Figure 1. Illustration of the problem with boundary (a) and representative heatlines visualization (b).

The local thermal equilibrium situation is considered among the solid porous structure and the hybrid nanofluid [51,55]. The Joule heating and Hall effect are assumed to be insignificant due to the smaller magnitude of induced magnetic Reynolds number (due to consideration of a lower range of magnetic strength and nanoparticles volume fraction) [5]. Also, the viscous dissipation and radiation effects are insignificant [55]. With the above consideration, the governing equations in dimensionless form can be stated as follows

$$\frac{\partial U}{\partial X}+\frac{\partial V}{\partial Y}=0 \tag{1}$$

$$\frac{1}{\varepsilon^2}\left(U\frac{\partial U}{\partial X}+V\frac{\partial U}{\partial Y}\right)=-\frac{\partial P}{\partial X}+\frac{\nu\,\mathrm{Pr}}{\nu_f\varepsilon}\left(\frac{\partial^2 U}{\partial X^2}+\frac{\partial^2 U}{\partial Y^2}\right)-\left(\frac{\nu\,\mathrm{Pr}}{\nu_f\mathrm{Da}}+\frac{F_c\sqrt{U^2+V^2}}{\sqrt{\mathrm{Da}}}\right)U+\frac{(\rho\beta)}{\rho\beta_f}\mathrm{Ra_m}\frac{\mathrm{Pr}}{\mathrm{Da}}\theta\sin\gamma \tag{2}$$

$$\frac{1}{\varepsilon^2}\left(U\frac{\partial V}{\partial X}+V\frac{\partial V}{\partial Y}\right)=-\frac{\partial P}{\partial Y}+\frac{\nu\,\mathrm{Pr}}{\nu_f\varepsilon}\left(\frac{\partial^2 V}{\partial X^2}+\frac{\partial^2 V}{\partial Y^2}\right)-\left(\frac{\nu\,\mathrm{Pr}}{\nu_f\mathrm{Da}}+\frac{F_c\sqrt{U^2+V^2}}{\sqrt{\mathrm{Da}}}\right)V-\frac{\rho_f}{\rho}\frac{\sigma}{\sigma_f}\lambda_B\mathrm{Ha}^2\,\mathrm{Pr}\,V+\frac{(\rho\beta)}{\rho\beta_f}\mathrm{Ra_m}\frac{\mathrm{Pr}}{\mathrm{Da}}\theta\cos\gamma \tag{3}$$

$$\left(U\frac{\partial\theta}{\partial X}+V\frac{\partial\theta}{\partial Y}\right)=\frac{\alpha}{\alpha_f}\left(\frac{\partial^2\theta}{\partial X^2}+\frac{\partial^2\theta}{\partial Y^2}\right) \tag{4}$$

where, $\rho c_p=$ specific heat capacity, $\rho\beta=$ thermal expansion coefficient, $k=$ thermal conductivity,$\sigma=$ electrical conductivity, are specified as

$$\rho=(1-\zeta)\rho_f+\zeta\,\rho_s,\quad \text{where } \zeta\rho_s=\zeta_{Al_2O_3}\rho_{Al_2O_3}+\zeta_{Cu}\rho_{Cu} \tag{5}$$

$$(\rho c_p)=(1-\zeta)(\rho c_p)_f+\zeta(\rho c_p)_s,\quad \text{where } \zeta(\rho c_p)_s=\zeta_{Al_2O_3}(\rho c_p)_{Al_2O_3}+\zeta_{Cu}(\rho c_p)_{Cu} \tag{6}$$

$$(\rho\beta)=(1-\zeta)(\rho\beta)_f+\zeta\,(\rho\beta)_s,\quad \text{where } \zeta\,(\rho\beta)_s=\zeta_{Al_2O_3}(\rho\beta)_{Al_2O_3}+\zeta_{Cu}(\rho\beta)_{Cu} \tag{7}$$

$$k=k_f\left[\frac{(k_s+2k_f)-2\zeta(k_f-k_s)}{(k_s+2k_f)+\zeta(k_f-k_s)}\right],\quad \text{where } \zeta k_s=\zeta_{Cu}k_{Cu}+\zeta_{Al_2O_3}k_{Al_2O_3} \tag{8}$$

$$\sigma=\sigma_f\left[1+\frac{3(\sigma_s/\sigma_f-1)\zeta}{(\sigma_s/\sigma_f+2)-(\sigma_s/\sigma_f-1)\zeta}\right],\quad \text{where } \zeta\sigma_s=\zeta_{Cu}\sigma_{Cu}+\zeta_{Al_2O_3}\sigma_{Al_2O_3} \tag{9}$$

$$\alpha=\frac{k}{(\rho c_p)} \tag{10}$$

$$\mu=\frac{\mu_f}{(1-\zeta)^{2.5}} \tag{11}$$

Here, ζ corresponds to the volumetric concentrations of hybrid nanoparticles (mixture of Al_2O_3 and Cu nanoparticles in the water) assuming $\zeta=\zeta_{Al_2O_3}+\zeta_{Cu}$. Table 1 listed the

Table 1. Water, Cu, and Al_2O_3 properties [58,64].

Properties	Water	Cu	Al_2O_3
c_p (Jkg^{-1} K^{-1})	4179	385	765
k (Wm^{-1} K^{-1})	0.613	401	40
α (kgm^{-3})	1.47×10^{-7}	1.11×10^{-4}	131.7×10^{-7}
β (K^{-1})	21×10^{-5}	1.67×10^{-5}	0.85×10^{-5}
ρ (kgm^{-3})	997.1	8933	3970
μ (kgm^{-1} s^{-1})	9.09×10^{-4}	–	–

Table 2. Experimental data of Cu-Al_2O_3/water hybrid nanofluid [58,61]

ζ (%)	$\zeta_{Al_2O_3}$ (%)	ζ_{Cu} (%)	μ(kgm^{-1} s^{-1})	k(Wm^{-1} K^{-1})
0.1	0.0962	0.0038	0.000972	0.619982
0.33	0.3175	0.0125	0.001098	0.630980
0.75	0.7215	0.0285	0.001386	0.649004
1.0	0.9620	0.0380	0.001602	0.657008
2.0	1.9241	0.0759	0.001935	0.684992

thermo-physical features of hybrid nanofluid. Similarly, the subscripts *f* and *s* corresponds to the carrier fluid (water) and solid nanopowder mixture (Cu and Al_2O_3). In this analysis, we have adopted dynamic viscosity, thermal and electrical conductivities (as listed in Table 2) from the actual measured data of Suresh et al. [61] instead of using the classical viscosity model [62] and thermal and electrical conductivity model [63]. This allows illustrating more accurate results.

In the momentum Equations (2) and (3), the term F_c $(= 1.75/\sqrt{150\varepsilon^3})$ resembles the Forchheimer coefficient (according to the Forchheimer-Brinkman-extended Darcy approach) in connection with porous medium permeability, K $(= \varepsilon^3 d_{ps}^2/150(1-\varepsilon)^2)$; where ϵ is porosity and d_{ps} is the average porous substance particle size [55]. Furthermore, the effective thermal diffusivityαin Equation (4) is calculated based on porosity-based expression $\alpha = (\varepsilon k + (1-\varepsilon)k_{ps})/(\rho C_P)$ [55,65,66]. This allows taking care of both the influence of thermal conductivities of working fluid (k) as well as porous material.

The dimensionless Equations (1)–(4) are attained defining the variables as

$$(X, Y) = (x, y)/H;\ (U, V) = (u, v)H/\alpha_f;$$
$$\theta = (T - T_c)/(T_h - T_c);\ P = (p - p_a)H^2/\rho\alpha_f^2 \tag{12a}$$

$$\mathrm{Pr} = \frac{\nu_f}{\alpha_f};\ \mathrm{Da} = \frac{K}{H^2};\ F_c = \frac{1.75}{\sqrt{150\varepsilon^3}};$$
$$\mathrm{Ra_m} = \frac{g\beta_f(T_h - T_c)KH}{\nu_f\alpha_f};\ \mathrm{Ha} = BH\sqrt{\sigma_f/\mu_f} \tag{12b}$$

The imposed boundary conditions for the present geometry are (in non-dimensional form)

The heat transfer characteristic is calculated using the average Nusselt number (Nu). Here, both the local as well as average Nu along the hot surface is estimated as:

$$\mathrm{Nu} = \frac{k}{k_f}\int_0^1 \left(-\frac{\partial\theta}{\partial X}\bigg|_{X=0,1}\right) dY \tag{13}$$

$$\begin{aligned} \theta &= 1 && \text{on the left heat source} \\ \theta &= 0 && \text{on the right cold wall} \\ \frac{\partial \theta}{\partial Y} &= 0 && \text{on the adiabatic walls} \end{aligned}$$

$$-\frac{\partial \psi}{\partial X} = V \quad \text{and} \quad \frac{\partial \psi}{\partial Y} = U \tag{14}$$

$$-\frac{\partial \Pi}{\partial X} = V\theta - \frac{k}{k_f}\frac{\partial \theta}{\partial Y} \quad \text{and} \quad \frac{\partial \Pi}{\partial Y} = U\theta - \frac{k}{k_f}\frac{\partial \theta}{\partial X} \tag{15}$$

The local fluid circulations, heat-energy transport phenomena, as well as temperature patterns, are visualized through the streamlines, heatlines, and isotherms, which are produced from the data set of velocity and temperature as obtained from the simulation. The streamlines are generated from the stream function ψ as expressed by Equation (14). Similarly, the heatlines are generated using the heat function (Π) [3,47,52,53].

3. Numerical procedure and validation study

In this study, finite volume method (FVM) based FORTRAN computing code has been applied to solve the dimensionless equations following the SIMPLE algorithm [67]. The domain geometry is divided into multiple sub-domains through staggered non-uniform mesh over which the discretized equations accompanied by the boundary conditions are solved in an iterative approach through the ADI (Alternating Direction Implicit) sweep technique and the TDMA (Tri-diagonal Matrix Algorithm) solver. For computing the convective terms (as in the momentum and energy Eqs.), a third-order upwind scheme QUICK (Quadratic Upstream Interpolation Convective Kinematics) is utilized. In addition, a second-order central differencing scheme is also adopted to handle the diffusion terms. The computation is carried out in an iterative process and the final converged solution is obtained when the relative error of the maximum residuals and the mass defect satisfies the convergence criterion of 10^{-8} and 10^{-10}, respectively [68]. In order to obtain a faster (less computation time) converged solution, successive over-relaxation (SOR) of the under-relaxed solutions is utilized. The various steps of the entire computation process are demonstrated through a flowchart of the code in Figure 2. This method has already been followed in our earlier works [47,69,70]. Lastly, the data set from the converged solutions are further processed for creating the contour plots and global values [71,72].

The present code has been used previously to validate various problems subjected to buoyant and mixed convection under diverse multiphysical circumstances [3,10,37,70] involving nanofluid, porous domain, magnetic field. Initially, the developed code has been validated with in-house experimental results of protruded heater cavity geometry [73]. However, another validation study is presented here by solving a benchmark problem of [74] and others [71]. The computed results of average Nu are equated with those of available results, which are listed in Table 3. This portrays that the applied code has a remarkable ability to solve a problem and it confirms the accuracy of the present code.

Further to the above, another validation study is also conducted by simulating the benchmark experimental results on a square cavity filled with alumina-water nanofluid

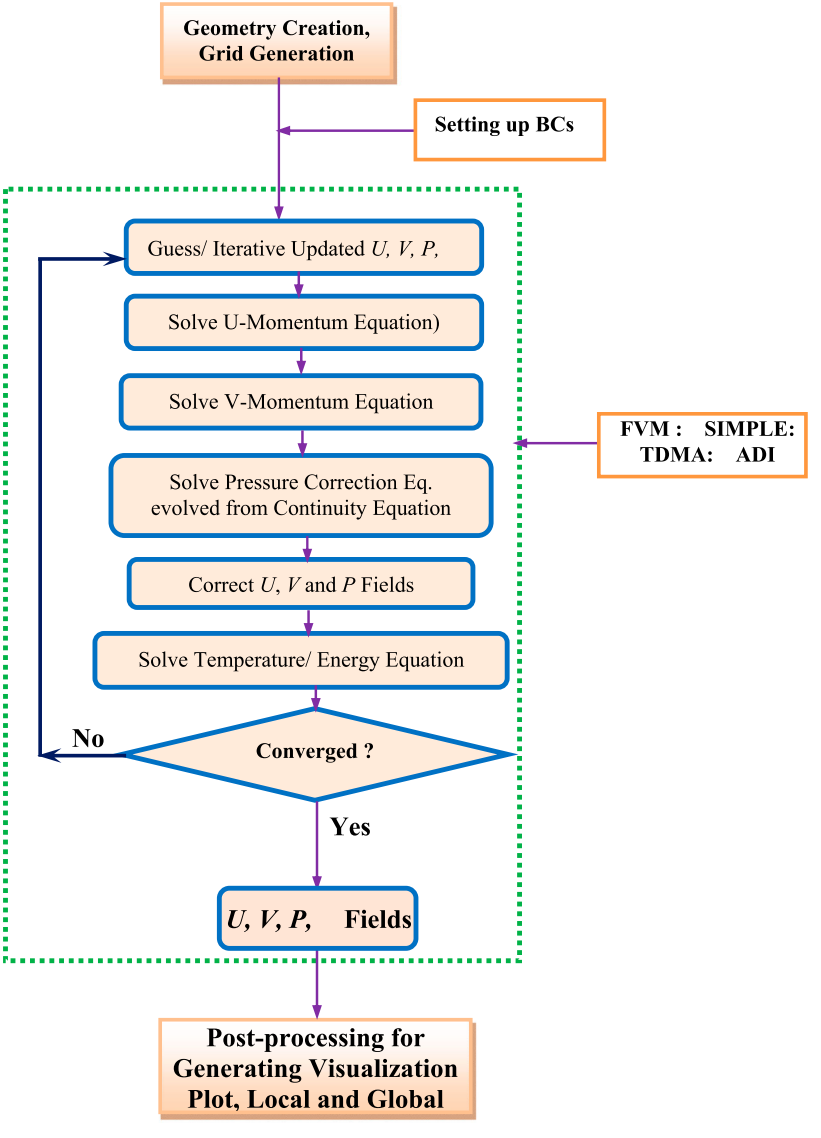

Figure 2. A flowchart demonstrating various steps of the entire computation process.

demonstrated by Ho et al. [76] as shown in Table 4. The comparison of mean Nusselt numbers is presented for the various temperature difference ($\Delta T = 4$–8°C) and nanoparticle concentrations ($\zeta = 0$ and 3%). The comparison shows that the present results are in good agreement with the published results in the absence of nanoparticles ($\zeta = 0$). However, with the increasing nanoparticle concentration, the difference is noted both in mean Nu values. In this study, the conventional Maxwell–Garnett's model for thermal conductivity and Brinkman's model for dynamic viscosity are utilized while the others use different models. Similar findings have also been reported by Sheikzadeh et al. [77].

Table 5 portrays the grid checking results for the varying Ra_m $(10 - 10^4)$ keeping $Da = 10^{-3}$, $Ha = 30$, $\gamma = 0°$, $\zeta = 0.1\%$ fixed. This checking is carried out for selecting the

Table 3. A benchmark validation study in terms of average Nu.

Ra	Present Results	De Vahl Davis [74]	Khanafer et al. [75]
10^3	1.115	1.118	1.118
10^4	2.251	2.243	2.245
10^5	4.545	4.519	4.522
10^6	8.846	8.799	8.826

Table 4. Experimental validation study through the mean Nusselt number (Nu), computed versus published experimental results [76] and numerical studies [77] for Test cell 1 ($L = 0.025$ m) for temperature difference ($\Delta T = 4$–$8°C$) and nanoparticle concentrations ($\zeta = 0$ and 3%).

	Mean Nusselt number (Nu) for $\zeta = 0$ (Water)			Mean Nusselt number (Nu) for $\zeta = 0.03$ (Nanofluid)		
ΔT (°C)	Present results	Ho et al. [76]	Sheikzadeh et al. [77]	Present results	Ho et al. [76]	Sheikzadeh et al. [77]
4	9.36	9.44	9.85	9.63	7.25	8.75
6	10.48	10.35	10.54	10.80	9.00	10.00
8	11.35	11.28	11.40	11.70	11.00	9.40

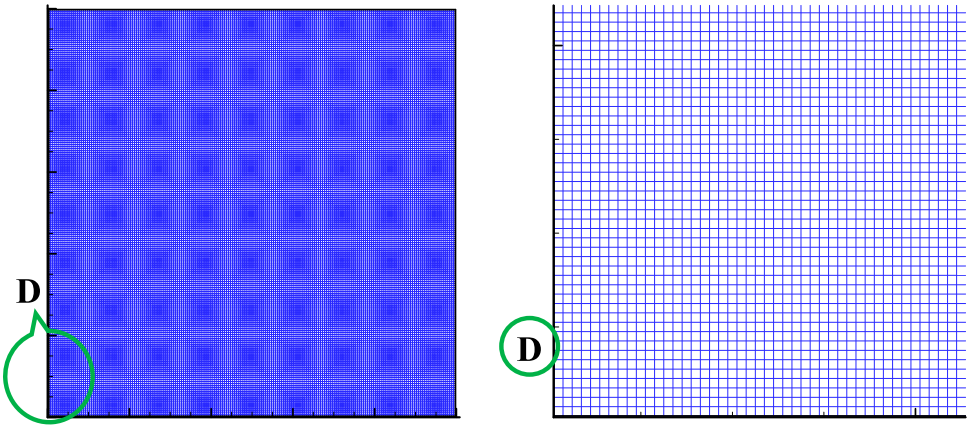

Figure 3. Mesh distribution for the present computational domain.

appropriate grids from different grid sizes (160×160, 200×200, and 240×240). The average Nu is estimated at the left hot wall ($X = 0$). Table 4 shows that successive error with 160×160 grids $< 1\%$ compared to the previous coarse grid. After 160×160 grids there is no substantial alteration in the Nu assessment and it shows very less order of error levels. From this test, 200×200 grid size is considered for further computations. Nevertheless, the grid dimension of 200×200 is preferred for the entire numerical simulations to afford additional grid points close to the boundary walls for capturing buoyancy-induced vortices in an improved technique. A typical distribution of mesh for the present computational domain is demonstrated in Figure 3 for $Ra_m = 10^3$, $Da = 10^{-3}$, $W_b = 0.4$, $Ha = 50$, $\zeta = 0.1\%$.

4. Results and discussion

The partially active middle-centered imposed magnetic fields' effect on the thermo-fluid behavior in an oblique enclosure packed with hybrid nanofluid is the aim of this study.

Table 5. Grid checking for $Ra_m = 10 - 10^4$ at $Da = 10^{-3}$, $Ha = 30$, $\gamma = 0°$,ζ 0.1%.

	Average Nusselt number (successive error in %)			
Ra_m	120×100	160×160	200×200	240×240
10	1.0243	1.0240 (0.03%)	1.0237 (0.03%)	1.0237 (0.0%)
10^2	2.1441	2.1420 (0.10%)	2.1410 (0.04%)	2.1408 (0.01%)
10^3	6.8909	6.8618 (0.42%)	6.8470 (0.22%)	6.8387 (0.12%)
10^4	14.8449	14.7579 (0.59%)	14.6751 (0.56%)	14.6276 (0.32%)

The problem of the present study is a varying inclined cavity filled with Cu/Al_2O_3-water hybrid nanofluids. It deals with multi-physical thermal systems due to the existence of porous substance, imposed magnetic field, and buoyancy effect due to side heating and side cooled wall. The impacts of different controlling parameters on the transport process are investigated extensively. For this, the study ranges are chosen as Darcy Rayleigh number ($Ra_m = 10, 10^2, 10^3, 10^4$), Darcy number ($Da = 10^{-5}, 10^{-4}, 10^{-3}, 10^{-2}, 10^{-1}$), Hartmann number ($Ha = 0, 10, 30, 50, 70$), width of the zone of active magnetic field ($W_b = 0, 0.2, 0.4, 0.6, 0.8, 1$), Cu-$Al_2O_3$-water hybrid nanofluid ($\zeta = 0, 0.1\%, 0.33\%, 0.75\%, 1\%, 2\%$), inclination angle of the cavity ($\gamma = 0°, 30°, 45°, 60°, 90°, 120°, 150°, 180°$), and a fixed porosity ($\varepsilon = 0.8$). The positional shifting of the partial magnetic fields is also included in the analysis. A comparison of no-magnetic field ($W_b = 0$), partial and whole domain ($W_b = 1.0$) magnetic field are also scrutinized. The results are explained by streamlines, isotherms, heatlines, and average Nusselt number in subsequent subsections.

4.1. Comparative assessment partial magnetic field over a no-magnetic field on the thermal performance

A comparative analysis of thermo-fluid flow-structures with streamlines, isotherms contour and heatlines, for fixed values of $Ra_m = 10^3$, $Da = 10^{-3}$, $Ha = 50$, $\zeta = 0.1\%$, and $\gamma = 0°$ under no-magnetic field ($W_b = 0$), partial ($W_b = 0.4$, with middle centered position) and whole domain ($W_b = 1$) magnetic field have been scrutinized and depicted in Figure 4. As a base cases study of such comparison in three columns, it is evidently observed that either whole domain or no-magnetic field reflects almost similar flow structures in streamlines, the static temperature distribution in comparison to the partial magnetic field. The flow pattern changes from inclined elliptic sizes to rhombus shapes with partial magnetic field with clockwise (CW) circulation. Rotational strength decreases from no-magnetic field to whole domain field as reflected from the first row of Figure 4. The circulation strength reducing rate is 11.05% to 34.24% for partial to no-magnetic in comparison to the applied magnetic field at $W_b = 1.0$. The heat flow features and also average Nu are improved with partial magnetic field compared to complete domain magnetic field. The importance of the base case study is intensified in the case of a partial magnetic field as shown in the 2nd column. Heat energy is transmitted to the cooled right sidewall whose sum-up value is total heat transmitted through the left heated wall. The recirculating energy cell is formed at the mid-zone of the cavity and accordingly, CW vortices are formed in the three cases with the shifting of the point of maximum energy strength with varying magnitude. Here, the energy flux strength increment rate is 11.47% to 33.87% for partial to a no-magnetic field in comparison to the applied magnetic field at $W_b = 1.0$. With the same parametric

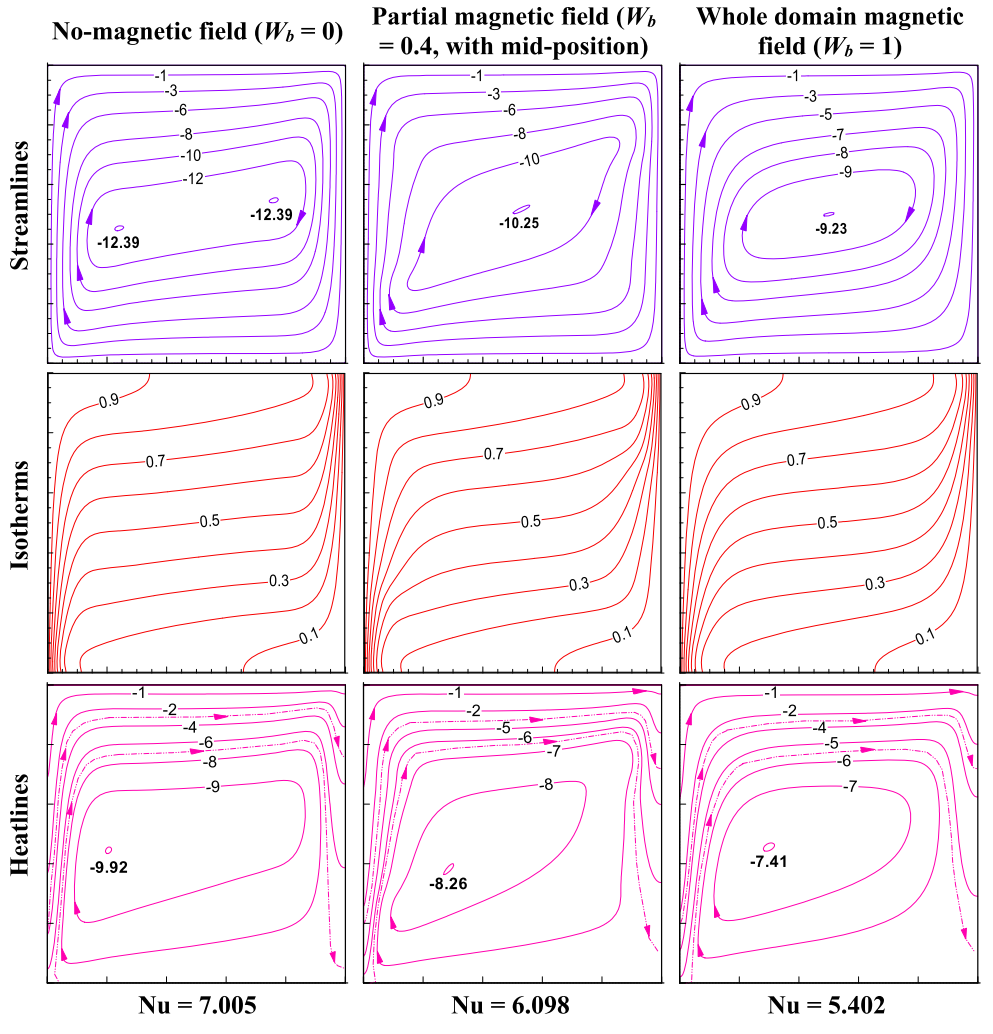

Figure 4. Comparison of partial magnetic field with no-magnetic field and full domain magnetic field through streamlines (first row), isotherms (second row) and heatlines contours (bottom row) for $\mathrm{Ra_m} = 10^3$, $\mathrm{Da} = 10^{-3}$, $\mathrm{Ha} = 50$, $\zeta = 0.1\%$, $\gamma = 0°$.

conditions, the heat transfer rate is being augmented for partial to a no-magnetic field in comparison to the applied magnetic field at $W_b = 1.0$ as denoted by the Nu value. In general, the heat exchange increment rate is 12.88% to 29.67% for partial to the absence of field in comparison to the whole domain magnetic field.

4.2. Impact of cavity inclination angle (γ)

A relative role of the inclination angle of the cavity on the thermo-fluid flow-structures under the middle-centered partially active magnetic fields (with $W_b = 0.4$) at $\mathrm{Ra_m} = 10^3$, $\mathrm{Da} = 10^{-1}$, $\mathrm{Ha} = 50$, and $\zeta = 0.1\%$ have been scrutinized as illustrated in Figure 5 for the range of cavity inclination γ (0°, 30°, 60°, 90°, 150°). The streamlines patterns are formed in the shape of discontinuous contours containing two separate core vortices (surrounded by

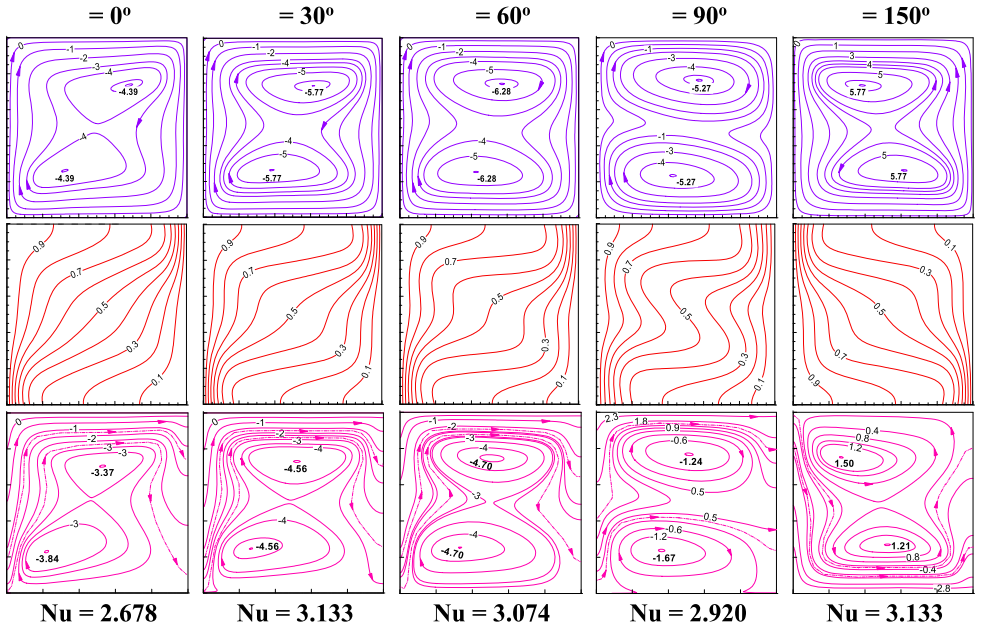

Figure 5. Effect of cavity inclination angle on streamlines (first row), isotherms (second row) and heatlines contours (bottom row) for $Ra_m = 10^3$, $Da = 10^{-2}$, $W_b = 0.4$, $Ha = 50$, $\zeta = 0.1\%$.

a large vortex) along the clockwise direction at the lower and upper part of the enclosure for all the cases (except $\gamma = 90°$). The separation of the circulating vortex happens owing to the presence of a partially active magnetic field about the horizontal middle-centered position of the enclosure. Under this zone of the magnetic field, fluid velocity drops substantially because of the strong opposing role of the Lorentz force to the buoyancy force. However, as the cavity angle rotates anti-clockwise direction, heat source and heat sink position relatively also change.

At $\gamma = 90°$ relation positions of the hot and cold walls are at the bottom and top respectively of the cavity. In this case, both the buoyancy force and magnetic force acts vertically. Buoyancy force strongly dominates the flow structure and it results in single circulation (CW) in the enclosure. Further increase in the cavity inclination angle, flow-structure again distorted and separated into circulating cells. However, rotation of the circulating cells changes from clockwise to anticlockwise direction due to changes in the relative position of the hot and cold walls. The average Nu decreases from 1.123 to 1.011 for $\gamma = 30°$ to $\gamma = 90°$ and corresponding fluid circulation strengths changes from 0.92 to 0.03. Further average Nu increases for $\gamma > 90°$, flow, temperature, and energy profile turns into an opposite sense of structure. However, at $\gamma = 90°$ the exception in the distributions of isotherm and heatlines are exactly vertical and horizontal respectively in comparison to other angles. Thus the transport process can be modulated significantly by varying the cavity inclination under the partial magnetic fields.

4.3. *Effect of partial magnetic field positions*

The allocation impacts of partial magnetic field on the fluid and energy flow pattern inside the tilted cavity have been investigated (in Figure 6). The active magnetic field length is

considered as $W_b = 0.4$ while $\mathrm{Ra_m} = 10^3$, $\mathrm{Da} = 10^{-3}$, $\mathrm{Ha} = 50$, $\zeta = 0.1\%$ and $\gamma = 45°$. Three different positions of the magnetic field over the left hot wall are chosen as the top (first column), middle (second column), and bottom (third column). With the top position of the partial magnetic field (with $W_b = 0.4$), the upper portion of the cavity fluid is subjected localized flow dampening effect. As a result, fluid flow faces more resistance in this zone. This effect is reflected by the distorted structures of the oval shape streamlines. Corresponding isotherms show clustering of isotherms adjacent to the active sidewalls and diagonal stretching over the entire cavity. Following the streamline patterns, heatlines contours also show a narrow passage for the heat energy transport from the hot to the cold wall, and the rest of the portion of the cavity is occupied by the recirculated energy cell. When the active zone of an imposed magnetic field is shifted to the middle-centered position of the left wall, flow resistance is generated about this zone. As a result, the flow structure is stretched diagonally from the top-left corner to the right-bottom corner. Static temperature distribution changes accordingly. Heatlines contours also show occupancy of the distorted energy recirculating cell and there is a narrow passage for the energy transport. Further lowering the magnetic position to bottom position, flow structure, temperature distribution, and heatlines contours show mirror changes compared to the top positioned magnetic field. However, the static temperature curvilinear allocations of isotherms contour in the three positions appear to be alike. The changes in the fluid circulation strengths are 16.86, 14.28, and 16.89 for the top, middle and bottom positions, respectively (as mentioned in the respective streamlines). Similarly, the passive energy recirculation strengths (11.93, 10.70, 12.08 for top, middle and bottom position respectively) considerably changes in heatline contours. The average Nu are 7.101, 6.847, and 7.110 for shifting the field intensity top, middle and bottom positions, respectively. For the tilted position of the cavity, the shape, size, strength, as well as the centers of all the circulations of fluid flow and heat energy circulation cells, are markedly affected by shifting the partial magnetic field. In general, the heat transfer, fluid, and energy recirculation strengths enhancement rate is about 3.71–3.84%, 18.07–18.28%, and 11.5–12.9% for top and bottom position, respectively compared to the middle position. Hence the shifting of the magnetic field's position alters the transport phenomena).

4.4. Effect of active length (W_b) of the partial magnetic field

In this section, the effect of active partial middle-centered magnetic fields length (W_b) normal to left sidewall has been analyzed as shown in Figure 7. The length of active partial magnetic fields are chosen as $W_b = 0.2$, 0.6 and 0.8 with fixed of $\mathrm{Ra_m} = 10^3$, $\mathrm{Da} = 10^{-3}$, $\mathrm{Ha} = 50$, $\zeta = 0.1\%$, $\gamma = 45°$. The pattern-wise streamlines appear as diagonally stretched ellipse and this is true for all cases of the partial magnetic field. Of course, as the length of the active magnetic field rises (keeping the same intensity of the magnetic field), the zone of magnetic field effect also increases, which causes a reduction in the flow velocity as well as heat energy-transportation over this zone. However, the uneven curvilinear distribution of temperature seems to be similar in the three cases. The intensity of the passive energy recirculation (11.72, 9.92, and 9.57 respectively for $W_b = 0.2$, 0.6, and 0.8 respectively) changes significantly in the heatline plots. The large energy recirculation cell shows some distinct features, particularly for the lower length W_b. The shape, strength, and centers of all circulating cells are substantially altered by changing the active length of the magnetic field. The

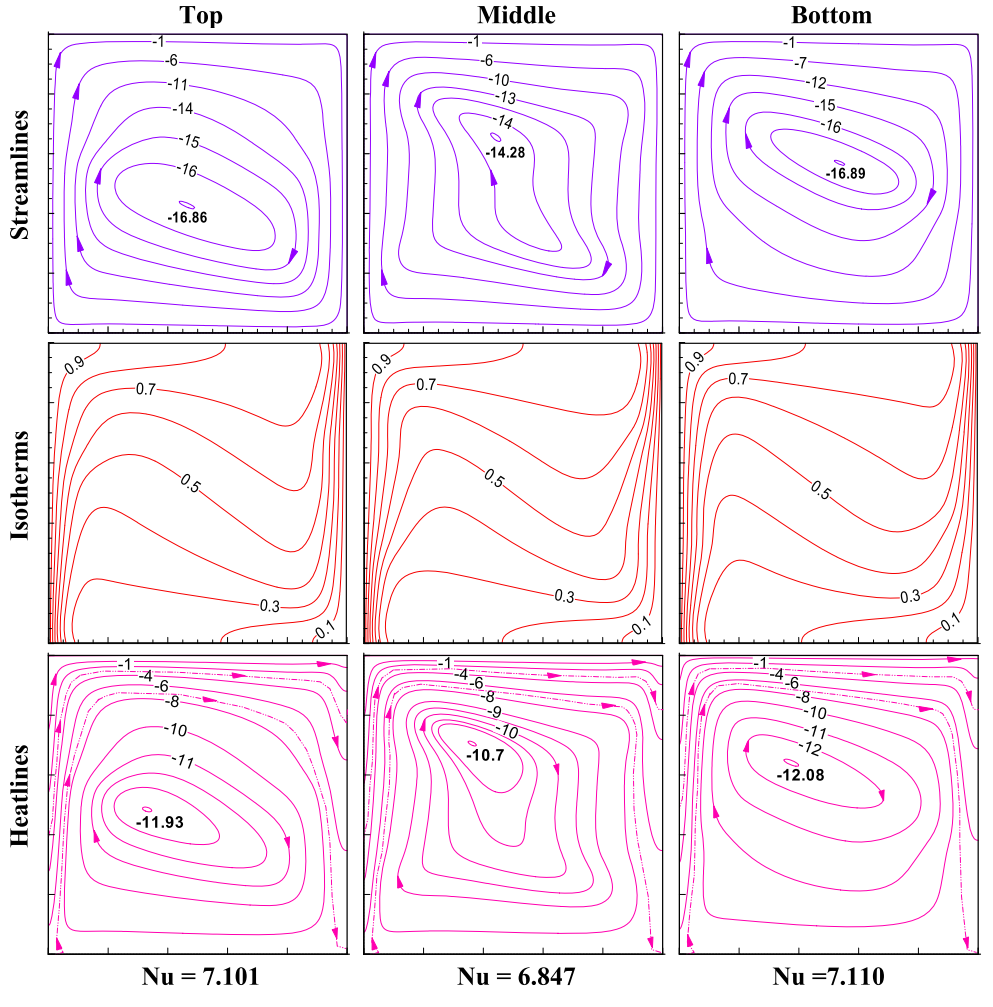

Figure 6. Role of partial magnetic field positions on streamlines (first row), isotherms (second row) and heatlines contours (bottom row) for $Ra_m = 10^3$, $Da = 10^{-3}$, $W_b = 0.4$, $Ha = 50$, $\zeta = 0.1\%$, $\gamma = 45°$.

value of average Nusselt number (Nu) increases as 6.174, 6.460 and 7.240 for W_b decreases 0.8, 0.6, and 0.2 respectively for the changes of the circulation strengths (12.93, 13.32 and 15.91 for $W_b = 0.8$, 0.6 and 0.2 respectively). These indicate that the transport process can also be governed by altering the magnetic field's length. In general, the heat transfer, flow circulation strengths, and energy recirculation strengths increasing rate is about 4.63–17.27%, 3.01–23.05%, and 3.12–21.83%, respectively for $W_b = 0.6$ and 0.2 compared to higher bandwidth W_b (= 0.8).

4.5. Effect of magnetic field intensity (Ha)

This section explores the role of the partially active magnetic fields (using dimensionless term Ha) strength are depicted in Figure 8 for the different values of Ha (0, 30, 70) for $R_{am} = 10^3$, $Da = 10^{-3}$, $W_b = 0.4$, $\zeta = 0.1\%$, $\gamma = 45°$. Here, $Ha = 0$ indicates no magnetic field, this has been discussed first to understand the flow physics relative to other values of

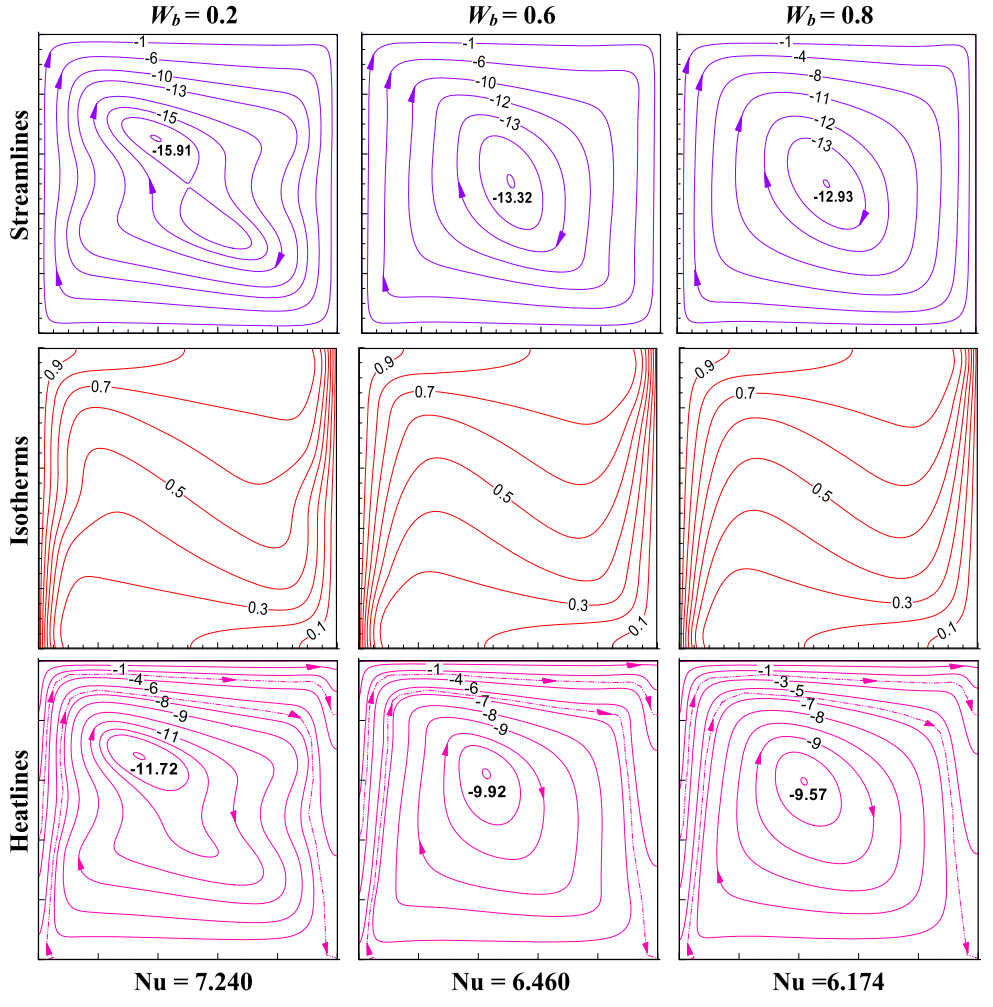

Figure 7. Impact of partial magnetic field positions on streamlines (first row), isotherms (second row) and heatlines contours (bottom row) for $Ra_m = 10^3$, $Da = 10^{-3}$, $Ha = 50$, $\zeta = 0.1\%$, $\gamma = 45°$.

Ha. Flow structure, as well as energy circulation cell, stretched diagonally from left-top corner to bottom-right corner. As expected, $Ha = 30$ weakens the dampening Lorentz force, there is no substantial change, noted on the flow-field and the average quantities of $|\psi|_{max}$ and average Nu. An almost similar pattern of flow structure is noted in the case of Ha of 0 and 30. But quite distinct features of contour structures are being observed at higher $Ha = 70$. About the mid-central plane of the cavity, a single circulating cell (both the fluid flow and energy cell) split into two, due to stronger magnetic force in this zone. Major changes in isotherms near active sidewalls are revealed due to alternatingly active magnetic fields, dampening effect is noted in circulation and recirculating energy cells also, thus the global parameters ($|\psi|_{max}$, $|\Pi|_{max}$, Nu) drops. Overall, the heat transfer, Nu, flow circulation strengths, $|\psi|_{max}$ and energy recirculation strengths $|\Pi|_{max}$ reduction rate is about 4.87–19.16%, 11.40–43.71%, and 9.17–33.40%, respectively for $Ha = 30$, 70 compared to the value at $Ha = 0$.

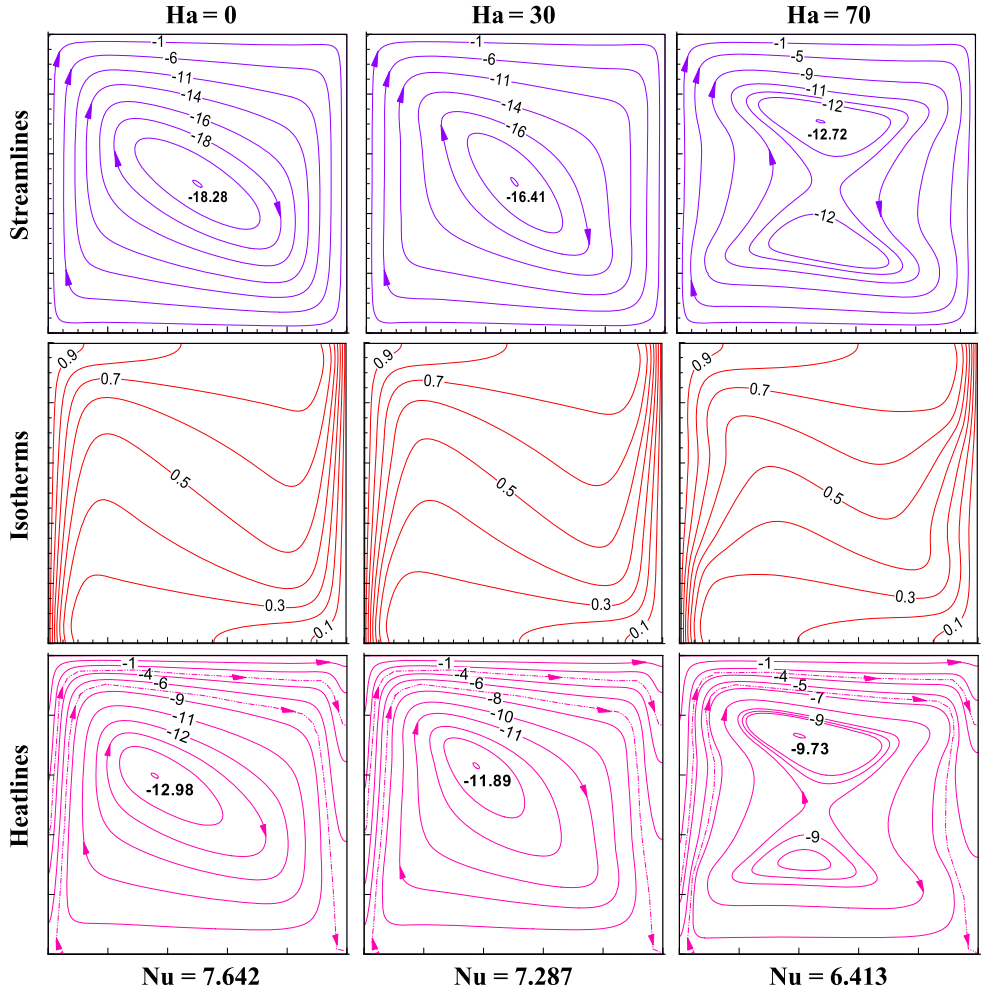

Figure 8. Influence of magnetic field intensity on streamlines (first row), isotherms (second row) and heatlines contours (bottom row) for $Ra_m = 10^3$, $Da = 10^{-3}$, $W_b = 0.4$, $\zeta = 0.1\%$, $\gamma = 45°$.

4.6. Effect of modified Rayleigh number (Ra_m)

This section highlights the role of low to higher Darcy–Rayleigh numbers ($Ra_m = 10$, 10^2 and 10^4) on thermo-physics in Figure 9 for fixed parameters ($Da = 10^{-3}$, $Ha = 50$, $\zeta = 0.1\%$, $\gamma = 45°$). This has been explored at constant effective length ($W_b = 0.4$) of partial magnetic fields by the streamlines, isotherms, heatlines, and the average Nu. An increase in Ra_m leads to the heightening of Ra (as $Ra_m = Ra \times Da$). Hence, at a fixed $Da = 10^{-3}$, the fluid Rayleigh number (Ra) emphasizes that the flow is moderately weaker at $Ra_m = 10$ (as $Ra = 10^4$) compared to that $Ra_m = 10^4$ (as $Ra = 10^7$). Here, most of the flow-patterns are intensely suffer as a result of varying Ra_m values for the same length and intensity of the magnetic field. The core zone shape of flow happens in the middle of the enclosure, vertical ellipse at $Ra_m = 10$, diagonal ellipse at $Ra_m = 10^2$, and parallelogram at $Ra_m = 10^4$ containing two recirculating core vortices. Fluid velocity takes a crucial role in thermal convection, the partial magnetic field equally contributes to the heat energy

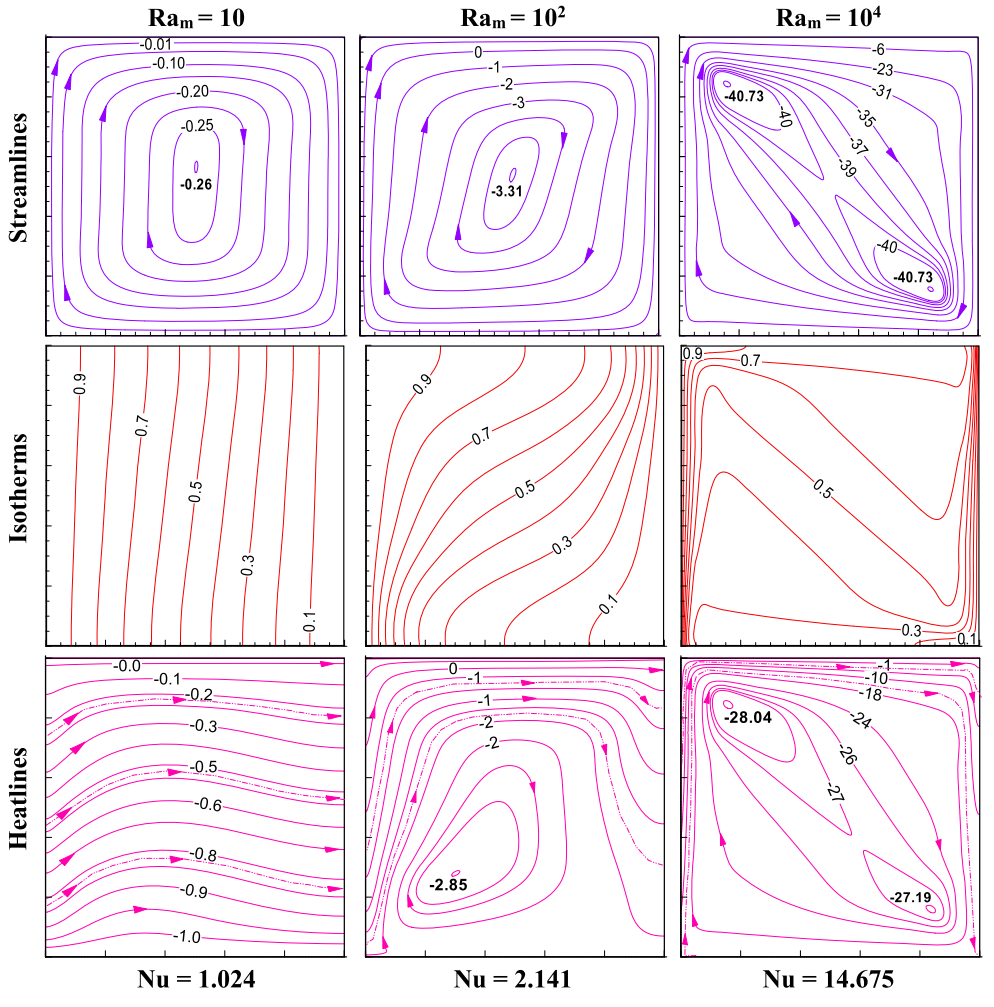

Figure 9. Effect of modified Rayleigh number (Ra_m) on streamlines (first row), isotherms (second row) and heatlines contours (bottom row) for Da $= 10^{-3}$, $W_b = 0.4$, Ha $= 50$, $\zeta = 0.1\%$, $\gamma = 45°$.

transport as shown by the heatlines, the passive heat energy recirculation cells are distinctly affected by the magnetic fields. Heatline corridors from the left heated sidewall to the right sidewall are noted in the energy cell. The average Nu also changes as 1.024, 2.141, and 14.675 for $Ra_m = 10, 10^2, 10^4$, respectively with the variations of the fluid flow strength (0.26, 3.31 and 40.73 for $Ra_m = 10, 10^2, 10^4$ respectively). The energy circulation strength increases markedly with the rise of Ra_m and the variations are prominent in the contours of heatlines. It is evident that the greater Darcy–Rayleigh number ($Ra_m = 10^4$) corresponds to rising global rates of flow ($|\psi|_{max}$) and heat transfer (Nu). In general, for $Ra_m = 10^2, 10^4$ the heat transfer, flow circulation strengths, and energy recirculation strengths increasing rate is about 52.19–93.03%, 92.15–99.36%, and 64.91–96.43%, respectively compared to lower $Ra_m = 10$. Therefore, the transport phenomena are affected by the Lorentz force in the active magnetic field because of the interaction between magnetic field and buoyancy force, inactive zone is having no impact on the magnetic dampening effect.

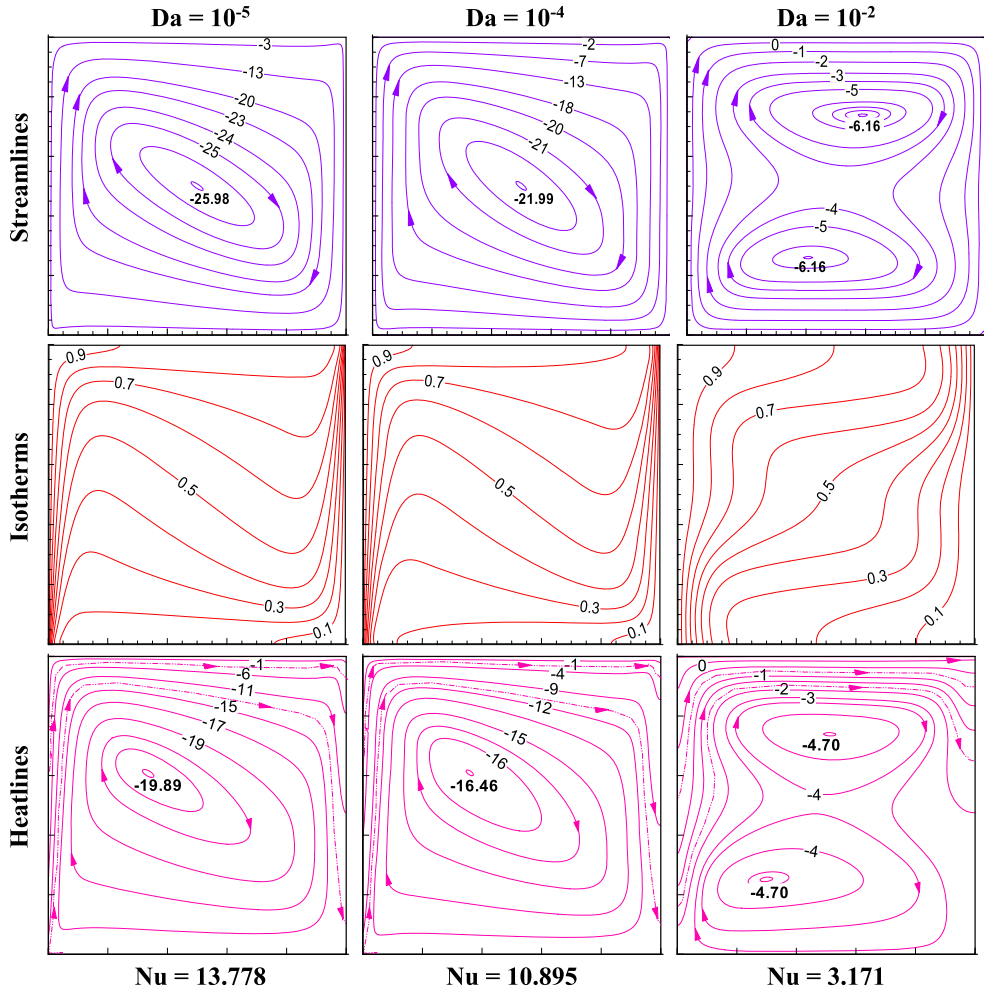

Figure 10. Influence of Darcy number (Da) on streamlines (first row), isotherms (second row) and heatlines contours (bottom row) for $Ra_m = 10^3$, $W_b = 0.4$, Ha = 50, $\zeta = 0.1\%$, $\gamma = 45°$.

4.7. Effect of Darcy number (Da)

The influence of the Darcy number (Da) with partial magnetic fields for $Ra_m = 10^3$, Ha = 50, $\zeta = 0.1\%$ and $\gamma = 45°$ are portrayed in Figure 10 for the range of Da (= 10^{-5}, 10^{-4}, 10^{-2}). It shows an inclined stretched large-sized vortex in both streamlines and heatlines is due to high resistive porous media at $Da = 10^{-5}$ in the stronger thermal convection ($Ra_m = 10^3$). As Da values intensify to $Da = 10^{-2}$, the fluid-based Ra drops that in turn alters the hydrodynamic state at different positions in the enclosure as shown in Figure 10. Thus, a single vortex is split into two irregular vortices as in the streamlines and heatlines plots. This is due to weaker convective flow under the partially active magnetic field. The circulating vortex at $Da = 10^{-5}$ forms an elliptical shape and stretches diagonally. The stretching is also noted the same for $Da = 10^{-4}$ and a single circulation in the cavity appear for $Da = 10^{-5}$ and $Da = 10^{-4}$ due to the applied localized magnetic field. All these effects are reflected in the heatline plots as it takes into consideration of both

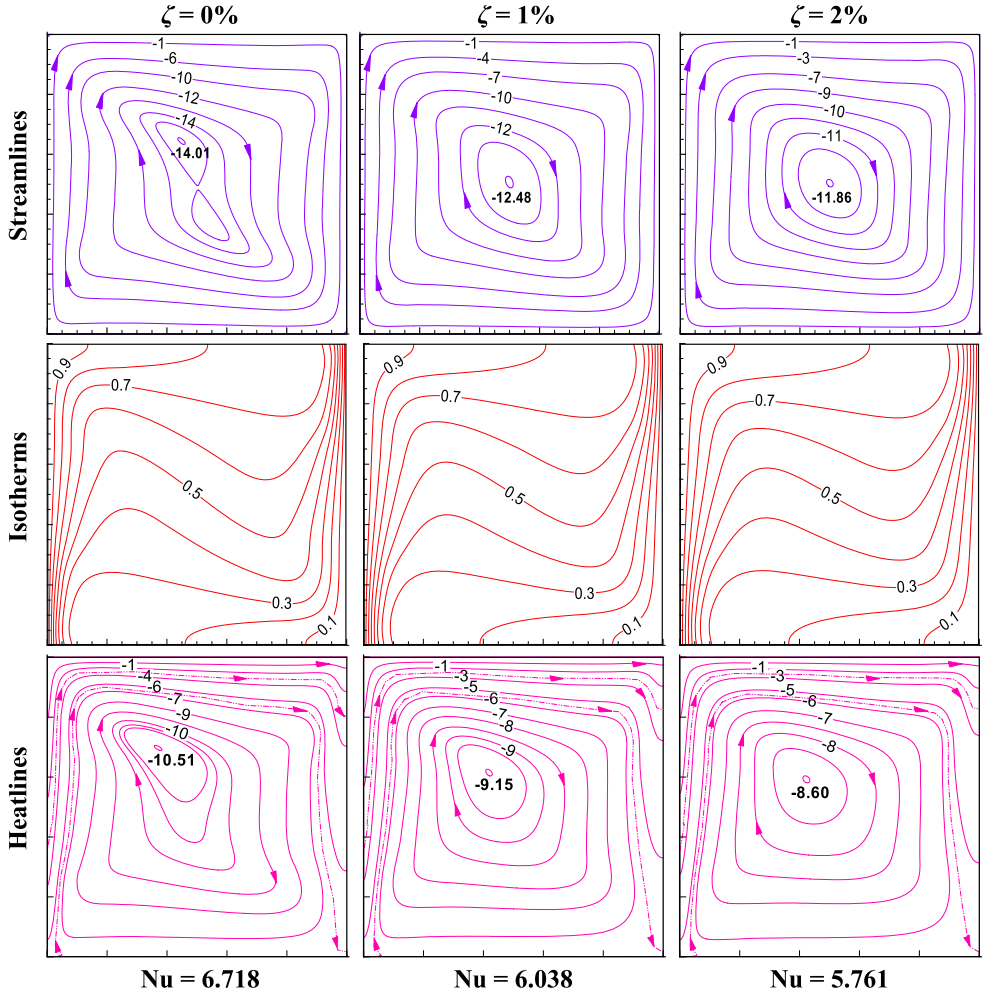

Figure 11. Effect of ζ on streamlines (first row), isotherms (second row) and heatlines contours (bottom row) for $\mathrm{Ra_m} = 10^3$, $\mathrm{Da} = 10^{-3}$, $W_b = 0.4$, $\mathrm{Ha} = 50$, $\gamma = 45°$.

convective and conductive heat fluxes. The heat transfer at $\mathrm{Da} = 10^{-2}$ is found relatively weaker, and thereby the flow structure and corresponding global parameters become less as mentioned by $|\psi|_{\max}$, $|\Pi|_{\max}$ and average Nu. In general, the heat transfer, flow circulation strengths, and energy recirculation strengths decrement rate is about 26.46–334.50%, 18.15–321.75%, and 20.84–323.19%, respectively for fixed $\mathrm{Ra_m} = 10^3$ compared to lower Da ($= 10^{-5}$).

4.8. Effect of hybrid nanoparticles volumetric concentration (ζ)

The impact of the hybrid nanoparticle volume concentration (ζ) on the thermo-fluid flow behavior under the partial magnetic field is shown in Figure 11 considering $\zeta = 0$, 1.0% and 2.0%, results have been computed at fixed parameters of $\mathrm{Ra_m} = 10^3$, $\mathrm{Da} = 10^{-3}$, $\mathrm{Ha} = 50$ and $\gamma = 45°$. As the hybrid nanoparticles concentration increases from 0% to 2%,

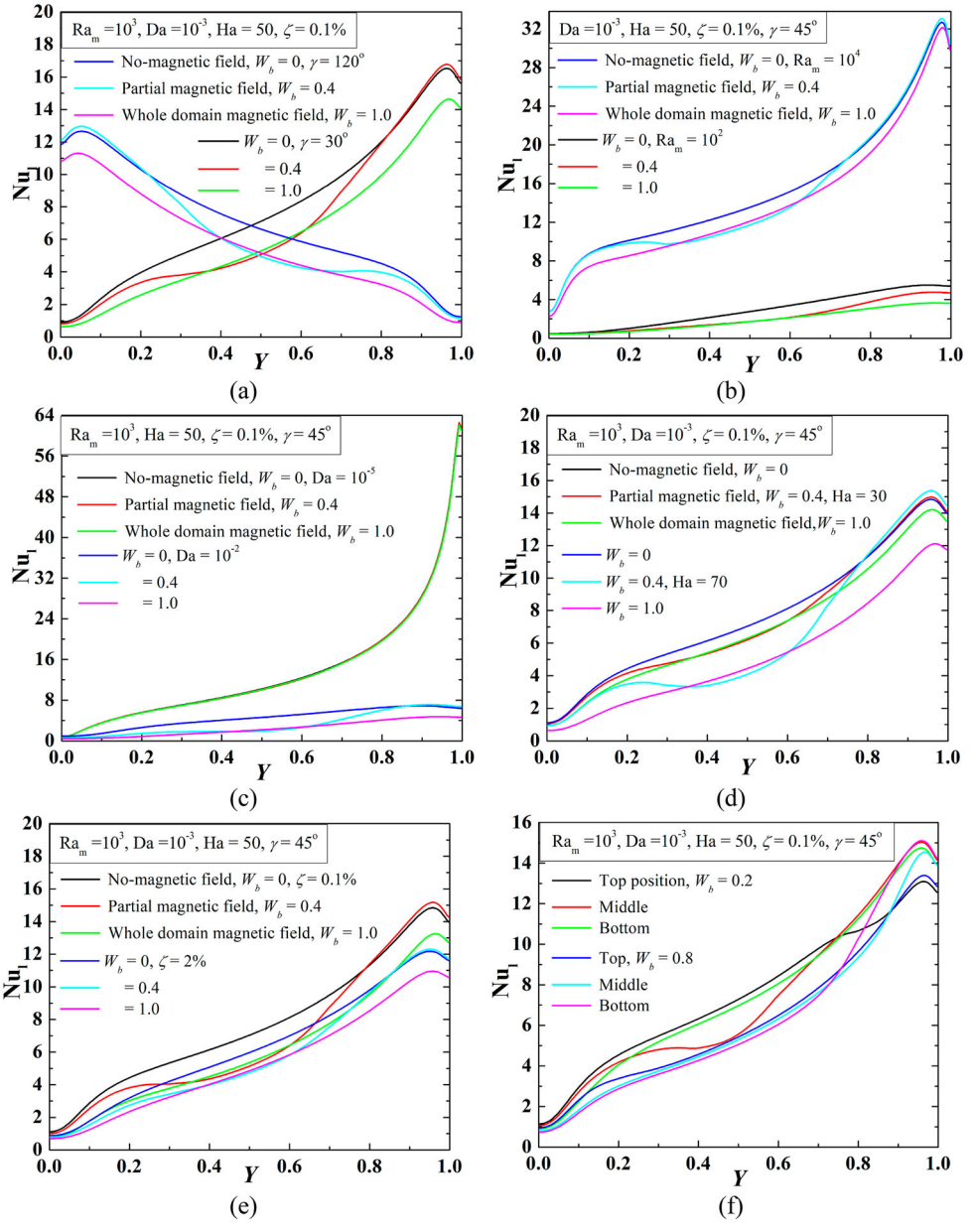

Figure 12. Variation of local heat transfer characteristics, Nu_l with (a) γ, (b) Ra_m, (c) Da, (d) Ha, (e) ζ, (f) W_b.

a decreasing trend of fluid-circulation strength and heat transfer in terms of Nu is clearly noted, this is caused by the substantial increase in viscosity of the fluid. The effects of partial magnetic field on thermo-fluid flow structure are distinctly reflected. In general, the heat transfer, flow circulation strengths, and energy recirculation strengths decrement rate is about 11.26–16.61%, 12.26–18.13%, and 14.86–22.21%, respectively compared to base fluid ($\zeta = 0$).

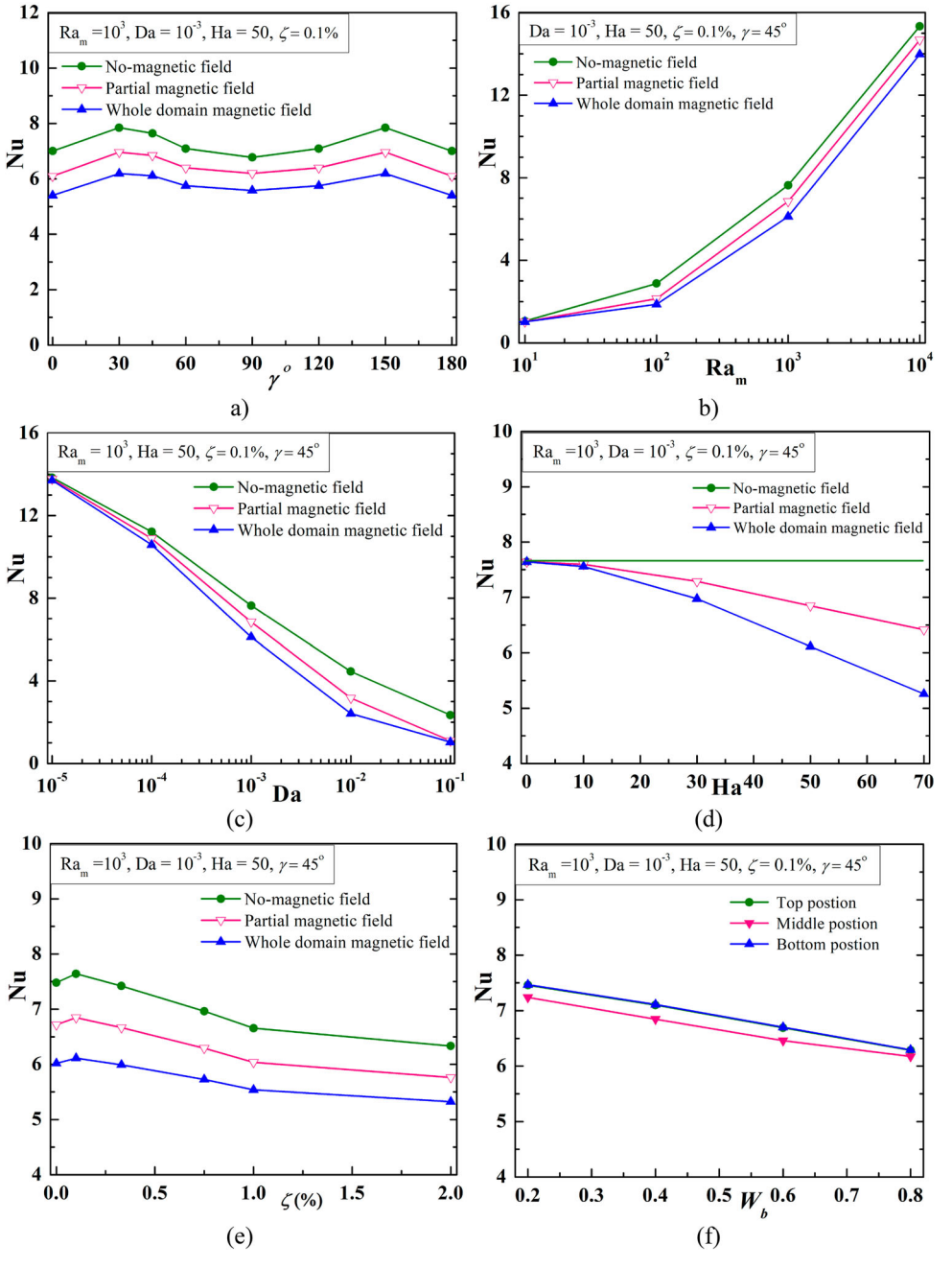

Figure 13. Variation of average Nu with (a) γ, (b) Ra_m, (c) Da, (d) Ha, (e) ζ, (f) W_b.

4.9. Assessment of heat transfer characteristics

The understanding of localized heat transfer uniqueness as designated by the local Nusselt number, Nu_l, for the heat sink (right side cold) wall is investigated under inequitable

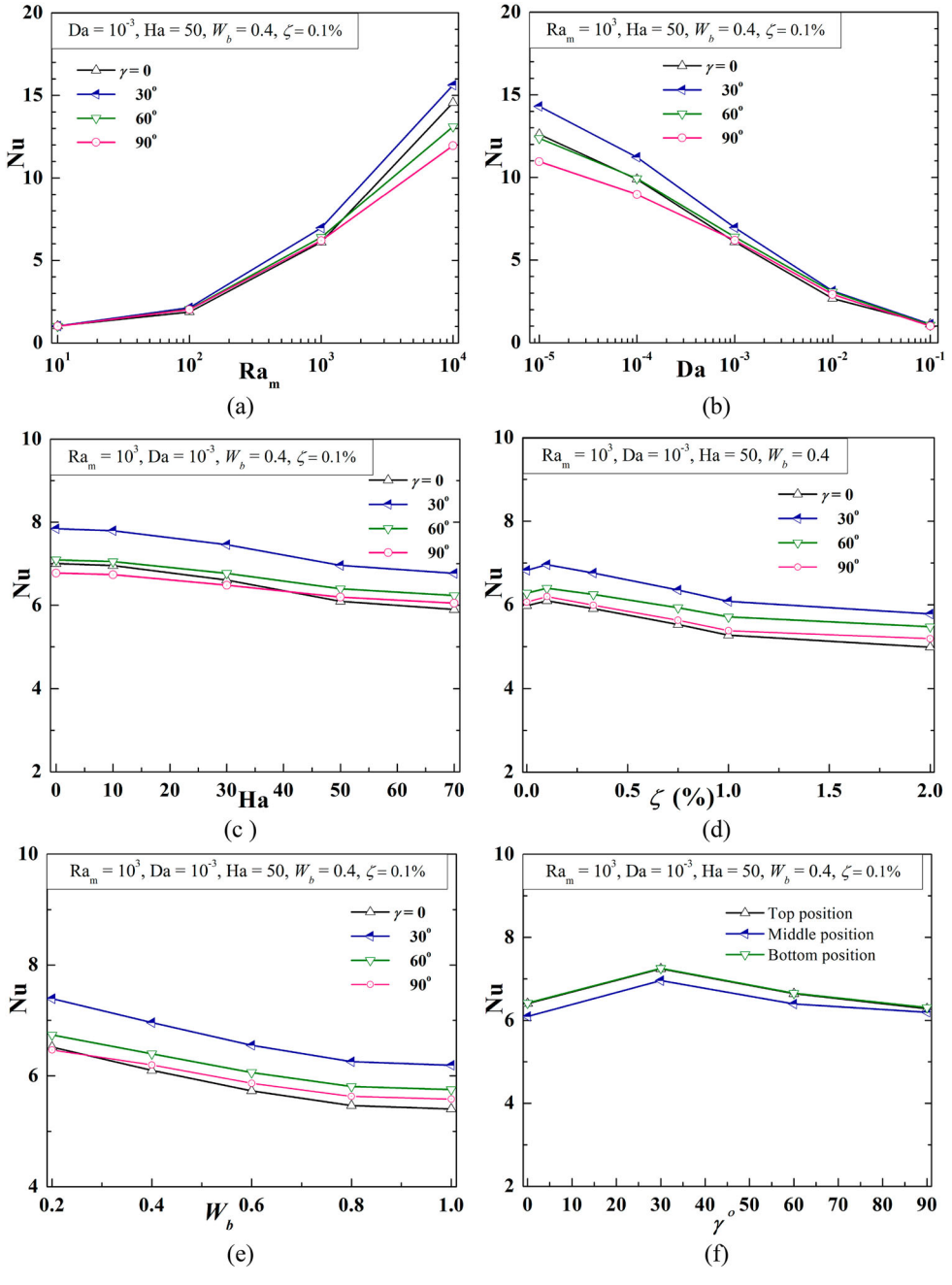

Figure 14. Heat transfer characteristics in terms of average Nu varying (a) Ra_m, (b) Da, (c) Ha, (d) ζ, (e) W_b (f) position of the partial magnetic field.

influencing parameters such as the inclination of the cavity (γ), Darcy-Rayleigh number (Ra_m), Hartmann number (Ha), Darcy number (Da), hybrid nanofluid volume fraction (ζ) for varying W_b and positional shifting as shown in Figure 12(a–f).

This shows local Nu comparison for no-magnetic field, partial and full domain magnetic field ($W_b = 0, 0.4, 1$) with two cavity angle $\gamma = 30°$ and $\gamma = 120°$, $Ra_m = 10^2$ and 10^4, Da $= 10^{-5}$ and 10^{-2}, Ha $= 30$ and 70, $\zeta = 0.1\%$ and 2% respectively by Figure 12(a–e). Figure 10(f) shows the effect of the top, middle, bottom positioned magnetic field for $W_b = 0.2$ and 0.8. It is observed that a peak of Nu_l is significantly produced near the top adiabatic wall which denotes the maximum Nu value. Two opposite natures of Nu curves are noted at angle $\gamma = 30°$ and 120°. Figure 12(b) shows local Nu comparison for no-magnetic field, partial and full magnetic field ($W_b = 0, 0.4, 1$) at $Ra_m = 10^2$ and 10^4. Local Nu with non-magnetic field case shows higher magnitude relative to whole domain magnetic field, whereas Nu with partial magnetic field remains in-between the two. This fact clearly reflects less reduction in Nu_l for the partial magnetic field relative to the full domain magnetic field. In other plots of Nu_l, similar natures of Nu are noted except its value. Almost the same curvilinear variations are reflected in both the cases (without magnetic field and full domain magnetic field) for all plots (Figures 10(e) to 12(a)). Local Nu value decreases in the mid-zone of cold sink wall such that curve becomes bend down in that zone due to impact of middle centered partial magnetic field. This is also reflected in the case of middle-centered magnetic field position (Figure 12(f)) in the same manner as earlier local Nu distribution. Two opposite natures of curves are noted at $\gamma = 30°$ and $\gamma = 120°$.

The graphical arrangement of the overall heat transfer characteristics as indicated by average Nu are explored under various influencing parameters such as γ, Ra_m, Da, Ha, ζ for varying W_b and its positional shifting as shown in Figure 13. As expected, this is observed that in all graphical plots, the maximum heat transfer average Nu values are reflected mostly for the enclosure position with a no-magnetic field. Figure 13(a) exemplifies the undulated magnitude of Nu with increasing cavity angle, $\gamma = 0$–180° for the fixed value of $Ra_m = 10^3$, Da $= 10^{-3}$, Ha $= 50$, $\zeta = 0.1\%$. Three undulated Nu curves for varying the inclination are represented in absence of magnetic field, partial and whole domain magnetic fields. The heat exchange rate increases from the horizontal cavity ($\gamma = 0°$) to $\gamma = 30°$, then consistently Nu decreases up to the vertical-cavity ($\gamma = 90°$), again increases when $\gamma = 150°$ and ultimately reduces in the inverted cavity position $\gamma = 180°$. It is evident that almost the same average Nu values are replicated for $\gamma = 0°$ and 180°, $\gamma = 30°$ and 150°, $\gamma = 60°$ and 120°. This is why the wavy pattern of the Nu curves is almost symmetrically propagated about $\gamma = 90°$. This stated variation seems to be similar for all kinds of partial magnetic fields.

Figure 13(b) exemplifies the rising value of Nu with rising Ra_m for Da $= 10^{-3}$, Ha $= 50$, $\zeta = 0.1\%$, $\gamma = 45°$. The convection system is completely assigned by the value of Ra_m states the computational domain, which is evidently emphasized in the Nu value and plotted for no-magnetic, partial, and whole domain magnetic fields. In addition, there is a minor effect of Ra_m on Nu till $Ra_m \leq 10^2$. Conversely, average Nu considerably rises with higher Ra_m and at upper Ra_m, the gap between the Nu curves grows monotonically. Such, growing trends are clearly observed for any length of the partial magnetic field ($W_b = 0, 0.4, 1$). Higher $Ra_m > 10^2$, heat transfer is superior. Furthermore, the difference between the Nu curves for any length of the partial magnetic field grows continually with the increasing Ra_m. With the change in partial magnetic field width effect from full domain ($W_b = 1.0$) to partial ($W_b = 0.4$) and no-magnetic field ($W_b = 0$) at tilted position of cavity, $\gamma = 45°$, heat transfer improves in the range 0.41–3.12% ($Ra_m = 10$), 14.91–54.28% (for $Ra_m = 10^2$), 12.0–25.0% (for $Ra_m = 10^3$) and 4.99–9.71% (for $Ra_m = 10^4$).

The impact of porous structure permeability on heat transport mechanism is described with variations of the Darcy number (Da $= 10^{-5}$ to 10^{-1}) for no-magnetic field, partial, full domain magnetic field ($W_b = 0, 0.4, 1$) keeping all other parameters fixed $\mathrm{Ra_m} = 10^3$, Ha $= 50$, $\zeta = 0.1\%$, $\gamma = 45°$ as shown in Figure 13(c). This displays that as the value of Da increase from 10^{-5}, the heat transfer decreases rapidly. In common, heat transfer enhances for partial ($W_b = 0.4$) and no-magnetic field ($W_b = 0$) in the range 0.48–0.96% (for Da $= 10^{-5}$), 2.95–6.02% (for Da $= 10^{-4}$), and 12.0–25.0% (for Da $= 10^{-3}$), 31.31–84.53% (for Da $= 10^{-2}$), and 6.52–126.59% (for Da $= 10^{-1}$) comparison to full domain magnetic field ($W_b = 1.0$).

From the role of magnetic field on the heat transfer characteristics (Figure 13(d)) for varying $W_b = 0, 0.4, 1$ at $\mathrm{Ra_m} = 10^3$, Da $= 10^{-3}$, $\zeta = 0.1\%$, $\gamma = 45°$, it is evident that no-magnetic field ($W_b = 0$) implies a horizontal line corresponds to Nu value for Ha $= 0$. The figure also shows a consistently dropping trend with the rising Ha for the other two cases of W_b. It is relevant that at lower Ha (< 10) heat transport mechanism is controlled by the stronger convection process, thus the magnetic field effect is not so prominent. Certainly, at the upper value of Ha ≥ 10, the energy transfer process is retarded due to the presence of stronger Lorentz forces, which dominate the convective process and it leads to a decrease in the heat transfer with the rising of Ha. Of course, at higher Ha, the generated force (extent of negative source term containing Ha in Y momentum equation) acts opposite to the buoyancy force. Therefore, the heat transfer mechanism can be modulated by adjusting the Ha value. So, the heat transfer augmentation rate for $W_b = 0.4$, partial band and no-magnetic field ($W_b = 0$) is about 0.51–1.11% (for Ha $= 10$), 5.51–9.6% (for Ha $= 30$) and 21.96–45.33% (for Ha $= 70$) relative to active magnetic field at $W_b = 1.0$.

The effect of heat transfer for different volumetric concentration of Cu/Al_2O_3-water hybrid nanofluid under no-magnetic field, imposed partial and whole domain magnetic field ($W_b = 0, 0.4, 1$) are reflected in the Figure 12(e) at $\mathrm{Ra_m} = 10^3$, Da $= 10^{-3}$, Ha $= 50$, $\gamma = 45°$. In this figure, $\zeta = 0$ corresponds to base fluid as pure water and also shows the maximum Nu value at $\zeta = 0.1\%$ in the Nu curve for all W_b. The inclusion of further hybrid nanoparticles clearly reveals a decreasing trend of Nu for any case. The heat transfer is less affected by the hybrid nanoparticles in the whole domain magnetic field. Inclusion of Cu/Al_2O_3 nanoparticles in pure water, the effective thermal conductivity of the fluid increases leading to an increase in the viscosity and decrement in thermal convection. Thus a lesser amount of heat is transported from the source to the sink. So the volume fraction of nanoparticles may be another parameter to control the heat transfer process. In general, the heat transfer decrement rate with the Cu/Al_2O_3 nanoparticles volume fraction ($\zeta = 0.33\%$ – 2%) about 0.83–18.13% (for $W_b = 0$, no-magnetic field), 0.77 to 16.62% (for $W_b = 0.4$, partial magnetic field), and 0.44–13.04% (for $W_b = 1.0$, whole domain magnetic field) compared to base fluid ($\zeta = 0$). The plot clearly establishes the use of hybrid nanofluid is effective from the heat transfer perspectives. From whole domain to partial and no-magnetic field stages, it is observed that Nu curves positioned in the upper region implying heat transport enhancement. Therefore, heat transfer growth rate for $W_b = 0.4$, partial band and no-magnetic field ($W_b = 0$) is about 11.62–24.30% ($\zeta = 0$, no particles), 11.26–23.83% (for $\zeta = 0.33\%$), 9.87–21.57% (for $\zeta = 0.75\%$), 9.03–20.18% (for $\zeta = 1\%$) and 8.2–18.95% (for $\zeta = 2\%$) compared to whole domain magnetic field, $W_b = 1.0$.

In addition, the effect of active zone of magnetic field length W_b ($= 0.2, 0.4. 0.6, 0.8$) on the heat transfer characteristics is shown in Figure 13(f) for shifting the partial magnetic field

position top, middle and bottom at $Ra_m = 10^3$, $Da = 10^{-3}$, $Ha = 50$, $\zeta = 0.1\%$, $\gamma = 45°$. The figure shows a consistently dropping trend with the rising W_b. It is relevant that at the middle position for all W_b, the heat transfer process is less, whereas that is almost the same for the top and bottom positions. Certainly, at the higher value of W_b, the intensity of magnetic fields is enhanced, which results in to decrease in the heat transfer. An increase in the active zone of the magnetic field with a rise in W_b acts against the buoyancy force. At all W_b, Nu curves shifted upper region for top and bottom band position in respect of mid position resulting increase in heat transfer rate. So, heat transfer increment rate is about 3.04–3.14% (for $W_b = 0.2$), 3.71–3.85% (for $W_b = 0.4$), 3.58–3.74% (for $W_b = 0.6$) and 1.78–1.94% (for $W_b = 0.8$) in the top and bottom position compared to middle band position of magnetic field. From the above heat transfer analysis, it is perceived that the active length of the applied partial magnetic field and its position significantly alters the overall thermal behavior of the enclosure, which is further affected by the involved flow controlling parameters. Further to these, we have noted that the orientation of the cavity also plays a significant role to affect thermal performance. This necessitates the investigation of the overall heat transfer under the varying cavity inclination angle, γ.

As described in Figure 14(a), average Nu values are repeated for $\gamma = 0°$ and 180°, $\gamma = 30°$ and 150°, $\gamma = 60°$ and 120° and symmetrically propagated about $\gamma = 90°$, so in this section, it has been selected to study heat exchange in respect of cavity angle in the range of $\gamma = 0°$ to 90°. Figure 14(a) epitomizes the heightening of average Nu with growing Ra_m for the fixed value of $Da = 10^{-3}$, $Ha = 50$, $W_b = 0.4$, $\zeta = 0.1\%$. With the cavity inclination $\gamma = 30°$, heat transfer improves 0.28% (for $Ra_m = 10$), 12.05% (for $Ra_m = 100$), 12.39% (for $Ra_m = 10^3$) and 6.79% (for $Ra_m = 10^4$) compared to the horizontal cavity $\gamma = 0°$.

The porous structure permeability in terms change in $Da = 10^{-5}$–10^{-1} is presented by varying cavity inclination ($\gamma = 0°$ to 90°) keeping fixed parameters as $Ra_m = 10^3$, $Ha = 50$, $W_b = 0.4$, $\zeta = 0.1\%$ as presented in Figure 14(b). The figure shows that the Nu decreases as the Da value increases for all tilting position. In general, with the cavity inclination $\gamma = 30°$ enhanced heat transfer compare to the horizontal cavity $\gamma = 0°$ in the range of 11.81% (for $Da = 10^{-5}$), 11.88% (for $Da = 10^{-4}$), 12.39% (for $Da = 10^{-3}$), 14.54% (for $Da = 10^{-2}$), and 0.45% (for $Da = 10^{-1}$).

Intensity of magnetic field specified by Ha on the diagram is shown in Figure 14(c) for any the directions ($\gamma = 0°$ to 90°) at $Ra_m = 10^3$, $Da = 10^{-3}$, $\zeta = 0.1\%$ with middle centered partial magnetic field ($W_b = 0.4$). The figure reflects a constant decreasing in Nu value with the increasing Ha. The heat transfer diminution rate is about 0.72–18.74% (with $\gamma = 0°$), 0.62–15.92% (with $\gamma = 30°$), 0.6–13.77% (with $\gamma = 60°$) and 0.58–11.99% (with $\gamma = 90°$) for $Ha = 10$–70, compared to $Ha = 0$, no-magnetic field.

The impact of volumetric fraction of hybrid nanofluid under any of the directions of partial ($W_b = 0.4$) magnetic field ($\gamma = 0°$ to 90°) are reflected in the Figure 14(d) at $Ra_m = 10^3$, $Da = 10^{-3}$, $Ha = 50$. In this figure, it is seen that by adding Cu/Al_2O_3 nanoparticles in pure water lesser quantity of heat is transported from the heated source to sink. Results, the heat transfer decrement rate varying with volume fraction ($\zeta = 0.33\%$ – 2%) about 1.19–19.86% (with $\gamma = 0°$), 0.97–18.09% (with $\gamma = 30°$), 0.51–14.7% (with $\gamma = 60°$) and 1.20–16.79% (with $\gamma = 90°$) compared to base fluid ($\zeta = 0$). It is interesting to see that at $\zeta = 0.1\%$ heat transfer enhancement is about 1.96% to 2.19% for $\gamma = 0°$ to 90° relative to base fluid ($\zeta = 0$).

Active length of the imposed magnetic field on the heat transfer distinctiveness is shown in Figure 14(e) for tilted cavity position ($\gamma = 0°$ to 90°) at fixed $\mathrm{Ra_m} = 10^3$, $\mathrm{Da} = 10^{-3}$, $\mathrm{Ha} = 50, \zeta = 0.1\%$. The figure shows a consistently dropping trend of heat transfer with the heightening width of the partial magnetic field. On the other hand, the heat transfer augmentation rate is about 1.15–20.7% (with $\gamma = 0°$), 1.03–19.4% (with $\gamma = 30°$), 0.93–17.1% (with $\gamma = 60°$) and 0.89–15.88% (with $\gamma = 90°$) in the range of bandwidth $W_b = 0.8$–0.2 compared to whole domain bandwidth ($W_b = 1.0$) of magnetic field.

Finally, Figure 14(f) reflects the impact of shifting active magnetic field position (with $W_b = 0.4$) for the different inclinations of the cavity ($\gamma = 0°$ to 90°). Top, middle and bottom – all three positions, it is seen that maximum Nu is obtainable at $\gamma = 30°$. The plot clearly establishes the middle position is effective in the lowest heat transfer point of view for all angular allocation of the cavity.

It is noteworthy to mention that a mathematical correlation is also developed through regression analysis (using MATLAB programming), to predict the overall heat transfer (using average Nu) involving various controlling parameters, which could be very useful for identifying the best operating parameters. The correlation for the average Nu for the range of buoyancy parameter ($\mathrm{Ra_m}$) and cavity orientation (γ) is expressed as

$$\mathrm{Nu} = b_1 + b_2\mathrm{Ra_m} + b_3\gamma + b_4\mathrm{Ra_m}\gamma + b_5\mathrm{Ra}_m^{0.5} \tag{16}$$

where the coefficients b_n is given by

b_1	b_2	b_3
0.635408394803562	−0.000231637753906	0.001716060817839
b_4	b_5	
−0.000003283034257	0.166249139212670	

The correlation for the average Nu for the range of porous media permeability (Da) and cavity orientation (γ) is expressed as

$$\mathrm{Nu} = b_1 + b_2\mathrm{Da} + b_3\gamma + b_4\mathrm{Da}\gamma + b_5\mathrm{Da}^{0.5} \tag{17}$$

where the coefficients b_n is given by

b_1	b_2	b_3
12.43714856	199.3751465	−0.012790655
b_4	b_5	
0.125637182	−98.95420932	

The correlation for the average Nu for the range of Lorentz force strength (Ha) and cavity orientation (γ) is expressed as

$$\mathrm{Nu} = b_1 + b_2\mathrm{Ha} + b_3\gamma + b_4\mathrm{Ha}\gamma + b_5\mathrm{Ha}^2 + b_6\gamma^{0.5} \tag{18}$$

where the coefficients b_n is given by

b_1	b_2	b_3
7.098475855240210	−0.017902348690539	−0.039619379322307
b_4	b_5	b_6
0.000072275396316	0.000000701794495	0.336622089327746

The correlation for the average Nu for the range of nanoparticle concentrations (ζ) and cavity orientation (γ) is expressed as

$$\mathrm{Nu} = b_1 + b_2\zeta + b_3\gamma + b_4\zeta\gamma + b_5{\zeta}^2 + b_6{\gamma}^{0.5} \tag{19}$$

where the coefficients b_n is given by

b_1	b_2	b_3
6.124290523	−94.62358818	−0.033618004
b_4	b_5	b_6
0.100536418	1826.356125	0.317573863

The correlation for the average Nu for the range of spatially active width of the partial magnetic field (W_b) considering the middle-middle position and cavity orientation (γ) is expressed as

$$\mathrm{Nu} = b_1 + b_2W_b + b_3\gamma + b_4W_b\gamma + b_5{W_b}^2 + b_6{\gamma}^{0.5} \tag{20}$$

where the coefficients b_n is given by

b_1	b_2	b_3
7.124426921015911	−3.054375820288397	−0.034368562682020
b_4	b_5	b_6
0.003574499982666	1.278458323445641	0.308017340810051

The correlation for the average Nu for the range of spatially active width of the partial magnetic field (W_b) considering the top-top position and cavity orientation (γ) is expressed as

$$\mathrm{Nu} = b_1 + b_2W_b + b_3\gamma + b_4W_b\gamma + b_5{W_b}^2 + b_6{\gamma}^{0.5} \tag{21}$$

where the coefficients b_n is given by

b_1	b_2	b_3
7.405379818900769	−2.797124557743901	−0.038935157351851
b_4	b_5	b_6
0.006783383312535	0.710700882558485	0.322791848761081

The correlation for the average Nu for the range of spatially active width of the partial magnetic field (W_b) considering the top-top position and cavity orientation (γ) is expressed as

$$\mathrm{Nu} = b_1 + b_2W_b + b_3\gamma + b_4W_b\gamma + b_5{W_b}^2 + b_6{\gamma}^{0.5} \tag{22}$$

where the coefficients b_n is given by

b_1	b_2	b_3
7.383757975719306	−2.692188058319177	−0.035822313553028
b_4	b_5	b_6
0.005436183315463	0.638075882921663	0.307428919533723

5. Conclusions

An innovative insight into the application of partial magnetic fields in an inclined cavity involving various multiphysical scenarios is presented in this work. The investigation is carried out considering convectional techniques of no-magnetic field and whole domain magnetic field, then the study is conducted by modified approach applying the partially active magnetic field under the various influencing factors like magnetic field strength, convective strength, permeability index, the concentration of Cu/Al_2O_3-water hybrid nanoparticles, positional shifting of an applied magnetic field, the orientation of the cavity. The convective system involves various multiphysics like thermal buoyancy, porous media, hybrid nanofluid, and magnetic field. Salient remarkable outcomes of the analysis are as follows:

- The principal outcomes specify that the application of a partially active magnetic field significantly alters the thermo-fluid flow pattern and heat-energy transportation compared to the no-magnetic and full domain magnetic field. The intensity of this change is found to soar with increasing Darcy-Rayleigh number, Darcy number, the concentration of hybrid nanoparticles, cavity incrimination angle, Hartmann number, and width of the active zone of a magnetic field. The technique of partial magnetic field is a better choice to achieve superior controllability of the convective transports effectively. This technique allows less reduction in heat transfer, which is $\sim$ 15% (with partial magnetic field) and $\sim$ 30% (with whole domain magnetic field) relative to the no-magnetic field.
- Moreover, the position, as well as width of the partial magnetic field, meaningfully controls the thermal behavior. It reflects that the middle-centered partial technique is of better choice and it can be a powerful control means for convective transport systems.
- Orientation of the enclosure has a noticeable impact on the overall thermal performance. The orientation of the cavity may be assigned to be 30° or 150° for achieving superior heat transfer in such a convective system.
- The local, as well as average heat transfer characteristics, are found to soar with the increasing modified Darcy-Rayleigh number; whereas it is decreasing function of Hartman number, Darcy number, hybrid nanoparticles concentration, etc. It is observed that a 0.1% concentration of hybrid nanoparticles is a better choice for boosting the heat transfer rate.
- A mathematical correlation is also developed through the regression analysis to predict the overall heat transfer involving various controlling parameters; which could be very useful for identifying the best operating parameters.

Convincingly, the above investigation undoubtedly emphasizes that the convective heat transfer process can be appreciably affected by changing of cavity angle imposing

magnetic field utilizing Cu-Al_2O_3 water hybrid nanofluid even in the existence of flow dampening porous structure and magnetic field. The entire investigation can afford valuable insight for controlling the heat transport process and physics of flow in a thermal enclosure and have a potential alternative of future work using under multi-physical conditions like porous media, varying hybrid nanoparticle, flow medium, position, and length of the partial magnetic field, etc.

Disclosure statement

No potential conflict of interest was reported by the author(s).

Funding

There is no financial support for this work.

ORCID

Milan K. Mondal http://orcid.org/0000-0003-2030-9753
Nirmalendu Biswas http://orcid.org/0000-0001-6304-6303
Dipak Kumar Mandal http://orcid.org/0000-0001-6361-2408
Nirmal K. Manna http://orcid.org/0000-0003-0913-864X
Ali J. Chamkha http://orcid.org/0000-0002-8335-3121

References

[1] Ganguly R, Sen S, Puri IK. Thermomagnetic convection in a square enclosure using a line dipole. Phys Fluids. 2004;16(7):2228–2236.
[2] Geridonmez BP, Oztop H.F. Natural convection in a cavity filled with porous medium under the effect of a partial magnetic field. Int J Mech Sci. 2019;161–162:105077:1–10.
[3] Manna NK, Mondal MK, Biswas N. A novel multi-banding application of magnetic field to convective transport system filled with porous medium and hybrid nanofluid. Phys Scr. 2021;96:065001.
[4] Barnothy MF, editer. Biological effects of magnetic fields. New York: Plenum Press, 1964.
[5] Davidson PA. An introduction to magnetohydrodynamics. Cambridge: Cambridge University Press; 2001.
[6] Christiansen MG, Howe CM, Bono DC, et al. Practical methods for generating alternating magnetic fields for biomedical research. Rev Sci Inst. 2017;88:084301.
[7] Puri IK, Ganguly R. Particle transport in therapeutic magnetic fields. Annu Rev Fluid Mech. 2014;46:407–440.
[8] Kappiyoor R, Liangruksa M, Ganguly R, et al. The effects of magnetic nanoparticle properties on magnetic fluid hyperthermia. J Appl Phys. 2010;108:094702.
[9] M'hamed B, Sidik NAC, Yazid MNAWM, et al. A review on why researchers apply external magnetic field on nanofluids. Int Commun Heat Mass Transfer. 2016;78:60–67.
[10] Manna NK, Biswas N. Magnetic force vectors as a new visualization tool for MHD convection. Int J Therm Sci. 2021;167:107004.
[11] Hamid M, Khan ZH, Khan WA, et al. Natural convection of water-based carbon nanotubes in a partially heated rectangular fin-shaped cavity with an inner cylindrical obstacle. Phys Fluids. 2019;31:103607.
[12] Khan ZH, Hamid M, Khan WA, et al. Thermal non-equilibrium natural convection in a trapezoidal porous cavity with heated cylindrical obstacles. Int Commun Heat Mass Transfer. 2021;126:105460.
[13] Khan ZH, Khan WA, Elbaz AMR, et al. Natural convection in triangular fin-shaped cavity with partially heated base using nanofluid. Z Angew Math Mech. 2021;101:e202000306.

[14] Bahiraei M, Jamshidmofid M, Goodarzi M. Efficacy of a hybrid nanofluid in a new microchannel heat sink equipped with both secondary channels and ribs. J Mol Liq. 2019;273:88–98.
[15] Tian Z, Arasteh H, Parsian A, et al. Estimate the shear rate & apparent viscosity of multi-phased non-Newtonian hybrid nanofluids via new developed support vector machine method coupled with sensitivity analysis. Physica A. 2019;535:122456.
[16] Anitha S, Safaei MR, Rajeswari S, et al. Thermal and energy management prospects of γ–AlOOH hybrid nanofluids for the application of sustainable heat exchanger systems. J Thermal Anal Calorim. 2021;1–7. Ahead-of-Print. DOI:10.1007/s10973-021-10996-9.
[17] Safaei MR, Karimipour A, Abdollahi A, et al. The investigation of thermal radiation and free convection heat transfer mechanisms of nanofluid inside a shallow cavity by lattice Boltzmann method. Physica A. 2018;509:515–535.
[18] Goodarzi H, Akbari OA, Sarafraz MM, et al. Numerical simulation of natural convection heat transfer of nanofluid with Cu, MWCNT, and Al_2O_3 nanoparticles in a cavity with different aspect ratios. J Thermal Sci Engg Appl. 2019;11:061020-1.
[19] Alazwari MA, Safaei MR. Combination effect of baffle arrangement and hybrid nanofluid on thermal performance of a shell and tube heat exchanger using 3-D homogeneous mixture model. Mathematics. 2021;9:881.
[20] Nazari S, Ellahi R, Sarafraz MM, et al. Numerical study on mixed convection of a non-Newtonian nanofluid with porous media in a two lid-driven square cavity. J Thermal Anal Calorim. 2020;140:1121–1145.
[21] Kabeel AE, El-Said EMS, Dafea SA. A review of magnetic field effects on flow and heat transfer in liquids: present status and future potential for studies and applications. Renew Sustain Energy Rev. 2015;45:830–837.
[22] Kumar A, Subudhi S. Preparation, characteristics, convection and applications of magnetic nanofluids: a review. Heat Mass Transfer. 2018;54:241–265.
[23] Pordanjani AH, Aghakhani S, Karimipour A, et al. Investigation of free convection heat transfer and entropy generation of nanofluid flow inside a cavity affected by magnetic field and thermal radiation. J Thermal Anal Calorim. 2019;137:997–1019.
[24] Nguyen-Thoi T, Sheikholeslami M, Hamid M, et al. CVFEM modeling for nanofluid behavior involving non-equilibrium model and Lorentz effect in appearance of radiation. Physica A. 2019;534:122154.
[25] Sheikholeslami M, Hamid M, Haq RU, et al. Numerical simulation of wavy porous enclosure filled with hybrid nanofluid involving Lorentz effect. Phys Scr. 2020;95:115701.
[26] Khan ZH, Khan WA, Sheremet MA, et al. Irreversibilities in natural convection inside a right-angled trapezoidal cavity with sinusoidal wall temperature. Phys Fluids. 2021;33:083612.
[27] Reddy PS, Sreedevi P. Effect of thermal radiation on heat transfer and entropy generation analysis of MHD hybrid nanofluid inside a square cavity. Waves Random Complex Media. 2022; 1–18. Ahead-of-Print. DOI:10.1080/17455030.2021.2003909.
[28] Sreedevi P, Reddy PS, Rao KVS. Effect of magnetic field and radiation on heat transfer analysis of nanofluid inside a square cavity filled with silver nanoparticles: Tiwari–Das model. Waves Random Complex Media. 2021; 1–19. Ahead-of-Print. DOI:10.1080/17455030.2021.1918798.
[29] Aghaei A, Sheikhzadeh GA, Goodarzi M, et al. Effect of horizontal and vertical elliptic baffles inside an enclosure on the mixed convection of a MWCNTs water nanofluid and its entropy generation. Eur Phys J Plus. 2018;133:486.
[30] Ebrahimi D, Yousefzadeh S, Akbari OA, et al. Mixed convection heat transfer of a nanofluid in a closed elbow–shaped cavity (CESC). J Thermal Anal Calorim. 2021;144:2295–2316.
[31] Yousefzadeh S, Rajabi H, Ghajari N, et al. Numerical investigation of mixed convection heat transfer behavior of nanofluid in a cavity with different heat transfer areas. J Thermal Anal Calorim. 2020;140:2779–2803.
[32] Goodarzi M, Safaei MR, Vafai K, et al. Investigation of nanofluid mixed convection in a shallow cavity using a two-phase mixture model. Int J Thermal Sci. 2014;75:204–220.
[33] Jamshed W, Nasir NAAM, Qureshi MA, et al. Dynamical irreversible processes analysis of Poiseuille magneto-hybrid nanofluid flow in microchannel: A novel case study. Waves Random Complex Media. 2021:1–23. Ahead-of-Print. DOI:10.1080/17455030.2021.1985185.

[34] Ahmed SE, Mansour MA, Mahdy A. Radiation and heat generation aspects on MHD convection of nanofluids in inclined wavy porous double lid-driven enclosures having obstacles: local thermal non-equilibrium. Waves Random Complex Media. 2021;1–18. Ahead-of-Print. DOI:10.1080/17455030.2021.2003909.
[35] Ghalambaz M, Sabour M, Sazgara S, et al. Insight into the dynamics of ferrohydrodynamic (FHD) and magnetohydrodynamic (MHD) nanofluids inside a hexagonal cavity in the presence of a non-uniform magnetic field. J Magn Magn Mater. 2020;497:166024.
[36] Ozoe H, Okada K. The effect of the direction of the external magnetic field on the three-dimensional natural convection in a cubical enclosure. Int J Heat Mass Transfer. 1989;32(10):1939–1954.
[37] Biswas N, Sarkar UK, Chamkha AJ, et al. Magneto-hydrodynamic thermal convection of $Cu–Al_2O_3$/water hybrid nanofluid saturated with porous media subjected to half-sinusoidal nonuniform heating. J Therm Anal Calorim. 2021;143:1727–1753.
[38] Biswas N, Manna NK, Chamkha AJ. Effects of half-sinusoidal nonuniform heating during MHD thermal convection in $Cu–Al_2O_3$/water hybrid nanofluid saturated with porous media. J Therm Anal Calorim. 2021;143:1665–1688.
[39] Al-Balushi LM, Rahman MM. Convective heat transfer utilizing magnetic nanoparticles in the presence of a sloping magnetic field inside a square enclosure. J Thermal Sci Eng Appl. 2019;11:041013-1–19.
[40] Jalil JM, Al-Tae'y KA. Natural convection in an enclosure under the influence of time-periodic magnetic field. Int J Appl Electromag Mech. 2009;31(2):97–111.
[41] Siddiqa S, Hossain MA, Gorla RSR. Conduction-radiation effects on periodic magnetohydrodynamic natural convection boundary layer flow along a vertical surface. Int J Thermal Sci. 2012;53:119–129.
[42] Mehryan SAM, Izadi M, Chamkha AJ, et al. Natural convection and entropy generation of a ferrofluid in a square enclosure under the effect of a horizontal periodic magnetic field. J Mol Liq. 2018;263:510–525.
[43] Jalil JM, Al-Tae'y KA, Ismail SJ. Natural convection in an enclosure with a partially active magnetic field. Numer Heat Transfer A. 2013;64(1):72–91.
[44] Szabo PSB, Früh W-G. The transition from natural convection to thermomagnetic convection of a magnetic fluid in a non-uniform magnetic field. J Magn Magn. Mater. 2018;447:116–123.
[45] Geridonmez BP, Oztop HF. Natural convection in a cavity under partial magnetic field applied from different corners. Int Commun Heat Mass Transfer. 2020;114:104575.
[46] Geridonmez BP, Oztop HF. MHD natural convection in a cavity in the presence of cross partial magnetic fields and Al_2O_3-water nanofluid. Comp Math Appl. 2020;80:2796–2810.
[47] Manna NK, Mondal C, Biswas N, et al. Effect of multibanded magnetic field on convective heat transport in linearly heated porous systems filled with hybrid nanofluid. Phys Fluids. 2021;33:053604.
[48] Al-Rashed AAAA, Kolsi L, Oztop HF, et al. 3D magneto-convective heat transfer in CNT-nanofluid filled cavity under partially active magnetic field. Physica E. 2018;99:294–303.
[49] Song KW, Tagawa T. Thermomagnetic convection of oxygen in a square enclosure under nonuniform magnetic field. Int J Thermal Sci. 2018;125:52–65.
[50] Jiang C, Shi E, Hu Z, et al. Numerical simulation of thermomagnetic convection of air in a porous square enclosure under a magnetic quadrupole field using LTNE models. Int J Heat Mass Transfer. 2015;91:98–109.
[51] Izadi M, Sheremet MA, Mehryan SAM. Natural convection of a hybrid nanofluid affected by an inclined periodic magnetic field within a porous medium. Chinese J Physics. 2020;65:447–458.
[52] Kimura S, Bejan A. The heatline visualization of convective heat transfer. J Heat Transfer. 1983;105:916–919.
[53] Biswas N, Mahapatra PS, Manna NK. Buoyancy-driven fluid and energy flow in protruded heater enclosure. Meccanica. 2016;51:2159–2184.

[54] Biswas N, Mondal MK, Manna NK, et al. Implementation of partial magnetic fields to magneto-thermal convective systems operated using hybrid-nanoliquid and porous media. J. Mech. Engg. Sci. 2021; 1–18. Ahead-of-Print. DOI:10.1177/09544062211060168.
[55] Nield DA, Bejan A. Convection in porous media. 3rd ed. Berlin: Springer; 2006.
[56] Biswas N, Mahapatra PS, Manna NK. Merit of non-uniform over uniform heating in a porous cavity. Int Commun Heat Mass Transfer. 2016;78:135–144.
[57] Manna NK, Biswas N, Mahapatra PS. Convective heat transfer enhancement: effect of multi-frequency heating. Int J Numer Meth Heat Fluid Flow. 2019;29(10):3822–3856.
[58] Ali HF. Hybrid nanofluids for convection heat transfer. 1st ed. Elsevier: Academic Press; 2020.
[59] Mandal DK, Mondal MK, Biswas N, et al. Nanofluidic thermal-fluid transport in a split-driven porous system working under a magnetic environment. Int J Numer Meth Heat Fluid Flow. 2021: 1–27. Ahead-of-Print. DOI:10.1108/HFF-08-2021-0555.
[60] Biswas N, Mondal MK, Mandal DK, et al. A narrative loom of hybrid nanofluid filled wavy walled tilted porous enclosure imposing a partially active magnetic field. Int J Mech Sci. 2022;217:107028.
[61] Suresh S, Venkitaraj K, Selvakumar P, et al. Effect of Al_2O_3–Cu/water hybrid nanofluid in heat transfer. Exp Thermal Fluid Sci. 2012;38:54–60.
[62] Brinkman HC. The viscosity of concentrated suspensions and solutions. J Chem Physics. 1952;20:571.
[63] Maxwell JC. A treatise on electricity and magnetism. Cambridge: Cambridge University Press; 1873.
[64] Ghalambaz M, Mehryan SAM, Izadpanahi E, et al. MHD natural convection of Cu–Al_2O_3 water hybrid nanofluids in a cavity equally divided into two parts by a vertical flexible partition membrane. J Therm Anal Calorim. 2019;138:1723–1743.
[65] Biswas N, Manna NK, Chamkha AJ, et al. Effect of surface waviness on MHD thermo-gravitational convection of Cu-Al2O3-water hybrid nanofluid in a porous oblique enclosure. Phys Scr. 2021;96:105002.
[66] Mandal DK, Biswas N, Manna NK, et al. Thermo-fluidic transport process in a novel M-shaped cavity packed with non-darcian porous medium and hybrid nanofluid: application of artificial neural network (ANN). Phys Fluids. 2022;34:033608.
[67] Patankar SV. Numerical heat transfer and fluid flow. New York (NY): Hemisphere; 1980.
[68] Mondal MK, Biswas N, Datta A, et al. Positional impacts of partial wall translations on hybrid nanofluid flow in porous media: real coded genetic algorithm (RCGA). Int J Mech Sci. 2022;217:107030.
[69] Mondal MK, Biswas N, Manna NK, et al. Enhanced magnetohydrodynamic thermal convection in a partially driven cavity packed with a nanofluid-saturated porous medium. Math Meth Appl Sci. 2021;1–28. DOI:10.1002/mma.7280.
[70] Biswas N, Manna NK, Datta P, et al. Analysis of heat transfer and pumping power for bottom-heated porous cavity saturated with Cu-water nanofluid. Powd Technol. 2018;326:356–369.
[71] Biswas N, Manna NK, Mukhopadhyay A, et al. Numerical simulation of laminar confined radial flow between parallel circular discs. J Fluids Engg. 2012;134:011205-1–8.
[72] Mondal MK, Biswas N, Manna NK. MHD convection in a partially-driven cavity with corner heating. SN Applied Sci. 2019;1:1689:1–1619.
[73] Biswas N, Mahapatra PS, Manna NK, et al. Influence of heater aspect ratio on natural convection in a rectangular enclosure. Heat Transfer Engg. 2016;37(2):125–139.
[74] Davis G. Natural convection of air in a square cavity, a benchmark numerical solution. Int J Numer Methods Fluids. 1962;3:249–264.
[75] Khanafer K, Vafai K, Lightstone M. Buoyancy-driven heat transfer enhancement in a two-dimensional enclosure utilizing nanofluids. Int J Heat Mass Transfer. 2003;46:3639–3653.
[76] Ho CJ, Liu WK, Chang YS, et al. Natural convection heat transfer of alumina-water nanofluid in vertical square enclosures: An experimental study. Int J Therm Sci. 2010;49:1345–1353.
[77] Sheikzadeh GA, Dastmalchi M, Khorasanizadeh H. Effects of nanoparticles transport mechanisms on Al_2O_3- water nanofluid natural convection in a square enclosure. Int J Therm Sci. 2013;66:51–62.